

# A study of the $P_{11}(1440)$ and $D_{13}(1520)$ resonances from CLAS data on $ep \rightarrow e'\pi^+\pi^-\rho'$

V.I. Mokeev,<sup>1,2,\*</sup> V.D. Burkert,<sup>1</sup> L. Elouadrhiri,<sup>1</sup> G.V. Fedotov,<sup>3,2</sup> E.N. Golovatch,<sup>2</sup> R.W. Gothe,<sup>3</sup> B.S. Ishkhanov,<sup>2</sup> E.L. Isupov,<sup>2</sup> K.P. Adhikari,<sup>31</sup> M. Aghasyan,<sup>20</sup> M. Anghinolfi,<sup>21</sup> H. Avakian,<sup>1</sup> H. Baghdasaryan,<sup>38</sup> J. Ball,<sup>10</sup> N.A. Baltzell,<sup>4</sup> M. Battaglieri,<sup>21</sup> V. Batourine,<sup>1</sup> I. Bedlinskiy,<sup>24</sup> A.S. Biselli,<sup>13,32</sup> C. Bookwalter,<sup>15</sup> S. Boiarinov,<sup>1,24</sup> W.J. Briscoe,<sup>17</sup> W.K. Brooks,<sup>36,1</sup> D.S. Carman,<sup>1</sup> A. Celentano,<sup>21</sup> G. Charles,<sup>10</sup> P.L. Cole,<sup>18,1</sup> M. Contalbrigo,<sup>19</sup> V. Crede,<sup>15</sup> A. D'Angelo,<sup>22,35</sup> A. Daniel,<sup>30</sup> N. Dashyan,<sup>40</sup> R. De Vita,<sup>21</sup> E. De Sanctis,<sup>20</sup> A. Deur,<sup>1</sup> C. Djalali,<sup>3</sup> D. Doughty,<sup>11,1</sup> R. Dupre,<sup>4,†</sup> A. El Alaoui,<sup>4</sup> P. Eugenio,<sup>15</sup> S. Fegan,<sup>37</sup> A. Fradi,<sup>23</sup> K.L. Giovanetti,<sup>25</sup> F.X. Girod,<sup>1</sup> W. Gohn,<sup>12</sup> L. Graham,<sup>3</sup> K.A. Griffioen,<sup>39</sup> B. Guegan,<sup>23</sup> M. Guidal,<sup>23</sup> L. Guo,<sup>14</sup> K. Hafidi,<sup>4</sup> H. Hakobyan,<sup>36,40</sup> C. Hanretty,<sup>38</sup> K. Hicks,<sup>30</sup> D. Ho,<sup>8</sup> M. Holtrop,<sup>28</sup> Y. Ilieva,<sup>3,17</sup> D.G. Ireland,<sup>37</sup> H.S. Jo,<sup>23</sup> K. Joo,<sup>12</sup> D. Keller,<sup>38</sup> M. Khandaker,<sup>29</sup> P. Khetarpal,<sup>14</sup> A. Kim,<sup>26</sup> W. Kim,<sup>26</sup> A. Klein,<sup>31</sup> F.J. Klein,<sup>9,1</sup> S. Koirala,<sup>31</sup> A. Kubarovsky,<sup>32,2</sup> V. Kubarovsky,<sup>1</sup> S.V. Kuleshov,<sup>36,24</sup> N.D. Kvaltine,<sup>38</sup> K. Livingston,<sup>37</sup> H.Y. Lu,<sup>8</sup> I. J. D. MacGregor,<sup>37</sup> Y. Mao,<sup>3</sup> N. Markov,<sup>12</sup> D. Martinez,<sup>18</sup> M. Mayer,<sup>31</sup> B. McKinnon,<sup>37</sup> C.A. Meyer,<sup>8</sup> T. Mineeva,<sup>12</sup> M. Mirazita,<sup>20</sup> H. Moutarde,<sup>10</sup> E. Munevar,<sup>1</sup> P. Nadel-Turonski,<sup>1</sup> C.S. Nepali,<sup>31</sup> A.I. Ostrovidov,<sup>15</sup> L.L. Pappalardo,<sup>19</sup> R. Parenduyan,<sup>40,‡</sup> K. Park,<sup>1,26</sup> S. Park,<sup>15</sup> E. Pasyuk,<sup>1</sup> S. Anefalos Pereira,<sup>20</sup> S. Pisano,<sup>20</sup> O. Pogorelko,<sup>24</sup> S. Pozdniakov,<sup>24</sup> J.W. Price,<sup>6</sup> S. Procureur,<sup>10</sup> D. Protopopescu,<sup>37</sup> B.A. Raue,<sup>14,1</sup> G. Ricco,<sup>16,§</sup> D. Rimal,<sup>14</sup> M. Ripani,<sup>21</sup> G. Rosner,<sup>37</sup> P. Rossi,<sup>20</sup> F. Sabatié,<sup>10</sup> M.S. Saini,<sup>15</sup> C. Salgado,<sup>29</sup> D. Schott,<sup>14</sup> R.A. Schumacher,<sup>8</sup> E. Seder,<sup>12</sup> H. Seraydaryan,<sup>31</sup> Y.G. Sharabian,<sup>1,40</sup> G.D. Smith,<sup>37</sup> L.C. Smith,<sup>38</sup> D.I. Sober,<sup>9</sup> D. Sokhan,<sup>23</sup> S. Stepanyan,<sup>1</sup> S.S. Stepanyan,<sup>26</sup> P. Stoler,<sup>32</sup> I.I. Strakovsky,<sup>17</sup> S. Strauch,<sup>3</sup> W. Tang,<sup>30</sup> C.E. Taylor,<sup>18</sup> Ye Tian,<sup>3</sup> S. Tkachenko,<sup>38</sup> A. Trivedi,<sup>3</sup> M. Ungaro,<sup>1,32</sup> M.F. Vineyard,<sup>33,34</sup> H. Voskanyan,<sup>40</sup> E. Voutier,<sup>27</sup> N.K. Walford,<sup>9</sup> M.H. Wood,<sup>7,3</sup> N. Zachariou,<sup>3</sup> Z.W. Zhao,<sup>38</sup> and I. Zonta<sup>22,¶</sup>  
(The CLAS Collaboration)

<sup>1</sup>Thomas Jefferson National Accelerator Facility, Newport News, Virginia 23606

<sup>2</sup>Skobeltsyn Nuclear Physics Institute and Physics Department at Moscow State University, 119899 Moscow, Russia

<sup>3</sup>University of South Carolina, Columbia, South Carolina 29208

<sup>4</sup>Argonne National Laboratory, Argonne, Illinois 60439

<sup>5</sup>Arizona State University, Tempe, Arizona 85287-1504

<sup>6</sup>California State University, Dominguez Hills, Carson, CA 90747

<sup>7</sup>Canisius College, Buffalo, NY

<sup>8</sup>Carnegie Mellon University, Pittsburgh, Pennsylvania 15213

<sup>9</sup>Catholic University of America, Washington, D.C. 20064

<sup>10</sup>CEA, Centre de Saclay, Irfu/Service de Physique Nucléaire, 91191 Gif-sur-Yvette, France

<sup>11</sup>Christopher Newport University, Newport News, Virginia 23606

<sup>12</sup>University of Connecticut, Storrs, Connecticut 06269

<sup>13</sup>Fairfield University, Fairfield CT 06824

<sup>14</sup>Florida International University, Miami, Florida 33199

<sup>15</sup>Florida State University, Tallahassee, Florida 32306

<sup>16</sup>Università di Genova, 16146 Genova, Italy

<sup>17</sup>The George Washington University, Washington, DC 20052

<sup>18</sup>Idaho State University, Pocatello, Idaho 83209

<sup>19</sup>INFN, Sezione di Ferrara, 44100 Ferrara, Italy

<sup>20</sup>INFN, Laboratori Nazionali di Frascati, 00044 Frascati, Italy

<sup>21</sup>INFN, Sezione di Genova, 16146 Genova, Italy

<sup>22</sup>INFN, Sezione di Roma Tor Vergata, 00133 Rome, Italy

<sup>23</sup>Institut de Physique Nucléaire ORSAY, Orsay, France

<sup>24</sup>Institute of Theoretical and Experimental Physics, Moscow, 117259, Russia

<sup>25</sup>James Madison University, Harrisonburg, Virginia 22807

<sup>26</sup>Kyungpook National University, Daegu 702-701, Republic of Korea

<sup>27</sup>LPSC, Université Joseph Fourier, CNRS/IN2P3, INPG, Grenoble, France

<sup>28</sup>University of New Hampshire, Durham, New Hampshire 03824-3568

<sup>29</sup>Norfolk State University, Norfolk, Virginia 23504

<sup>30</sup>Ohio University, Athens, Ohio 45701

<sup>31</sup>Old Dominion University, Norfolk, Virginia 23529

<sup>32</sup>Rensselaer Polytechnic Institute, Troy, New York 12180-3590

<sup>33</sup>Union College, Schenectady, NY 12308

<sup>34</sup>University of Richmond, Richmond, Virginia 23173

<sup>35</sup>Università di Roma Tor Vergata, 00133 Rome Italy

<sup>36</sup>Universidad Técnica Federico Santa María, Casilla 110-V Valparaíso, Chile

<sup>37</sup>University of Glasgow, Glasgow G12 8QQ, United Kingdom

<sup>38</sup>University of Virginia, Charlottesville, Virginia 22901

<sup>39</sup>College of William and Mary, Williamsburg, Virginia 23187-8795

<sup>40</sup>Yerevan Physics Institute, 375036 Yerevan, Armenia

(Dated: March 4, 2013)

The transition helicity amplitudes from the proton ground state to the  $P_{11}(1440)$  and  $D_{13}(1520)$  excited states ( $\gamma_v p N^*$  electrocouplings) were determined from the analysis of nine independent one-fold differential  $\pi^+ \pi^- p$  electroproduction cross sections off a proton target, taken with CLAS at photon virtualities  $0.25 \text{ GeV}^2 < Q^2 < 0.60 \text{ GeV}^2$ . The phenomenological reaction model was employed for separation of the resonant and non-resonant contributions to the final state. The  $P_{11}(1440)$  and  $D_{13}(1520)$  electrocouplings were obtained from the resonant amplitudes parametrized within the framework of a unitarized Breit-Wigner ansatz. They are consistent with results obtained in the previous CLAS analyses of the  $\pi^+ n$  and  $\pi^0 p$  channels. The successful description of a large body of data in dominant meson-electroproduction channels off protons with the same  $\gamma_v p N^*$  electrocouplings offers clear evidence for the reliable extraction of these fundamental quantities from meson-electroproduction data. This analysis also led to the determination of the long-awaited hadronic branching ratios for the  $D_{13}(1520)$  decay into  $\Delta\pi$  (24%-32%) and  $N\rho$  (8%-17%).

PACS numbers: 11.55.Fv, 13.40.Gp, 13.60.Le, 14.20.Gk

## I. INTRODUCTION

An extensive research program on nucleon resonance ( $N^*$ ) excitation is in progress using the CLAS detector in Hall-B at Jefferson Lab [1–5]. The studies of transition helicity amplitudes from the proton ground state to its excited states (or  $\gamma_v p N^*$  photo-/electrocouplings) represent a key direction in the  $N^*$  program with CLAS. Meson-electroproduction data off nucleons in the  $N^*$  region obtained with CLAS open up an opportunity to determine the  $Q^2$ -evolution of  $\gamma_v N N^*$  electrocouplings in a combined analysis of various meson-electroproduction channels. The  $Q^2$ -evolution of  $\gamma_v N N^*$  electrocouplings will allow us to pin down active degrees of freedom in the  $N^*$  structure at various distance scales and to access non-perturbative strong-interaction mechanisms that govern the excited nucleon state formation as bound systems of quarks and gluons.

Theoretical and experimental studies of the electroexcitation of nucleon resonances have a long history. Along with the hadron masses and their partial decay widths, the information on the  $\gamma_v p N^*$  electrocouplings played an important role in the development of the quark models in their contemporary advanced relativistic version in light-front dynamics [8–14]. The picture of the nucleon and its excited states, which seemed quite simply modeled with three relativistic constituent quarks, turned out to be more complex. Recently obtained electrocouplings for the  $P_{11}(1440)$ ,  $D_{13}(1520)$ , and  $S_{11}(1535)$  states [15]

showed that those quark models, which were successful in describing the electrocouplings of these states for  $Q^2 > 2.0 \text{ GeV}^2$ , failed to reproduce the results at smaller photon virtualities of  $Q^2 < 1.0 \text{ GeV}^2$ . Quark models with flavor-conserving quark interactions are unable to describe the small mass of the  $P_{11}(1440)$  state [16] and the ordering of  $P_{11}(1440)$  and  $S_{11}(1535)$  resonances [1]. Moreover, models that treat the  $P_{11}(1440)$  structure as just three constituent quarks are unable to describe the large total  $P_{11}(1440)$  decay width of  $\approx 300 \text{ MeV}$ . These difficulties prompted a search for additional contributions to the  $N^*$  structure.

A general unitarity requirement imposes meson-baryon dressing contributions to both resonance electromagnetic excitation and hadronic decay amplitudes. Studies of meson-baryon dressing contributions to  $\gamma_v p N^*$  electrocouplings and resonance hadronic decay amplitudes, carried out at the Excited Baryon Analysis Center (EBAC) at Jefferson Lab [17–24], have extended our insight into the spectrum and structure of excited nucleon states considerably. The contributions from meson-baryon dressing to the  $P_{11}(1440)$  and  $D_{13}(1520)$  electrocouplings were determined from a global analysis of the world data on  $\pi N$  scattering and  $\pi^+ n$ ,  $\pi^0 p$  electroproduction off protons within the framework of the EBAC dynamical coupled-channel approach (EBAC-DCC) [23].

This analysis showed that the contributions from meson-baryon dressing to the  $\gamma_v p N^*$  electrocouplings are maximal at small  $Q^2$  and decrease with increasing photon virtualities [17]. At  $Q^2 < 1.0 \text{ GeV}^2$  these contributions may even be dominant. The meson-baryon cloud has a profound impact on the resonance spectrum. For example, in the  $P_{11}$  partial wave a single bare resonance pole located at  $W=1.76 \text{ GeV}$ , being affected by meson-baryon dressing, splits into three poles located on different Riemann sheets [21, 22]. Two of them with  $Re(W) \approx 1.36 \text{ GeV}$  correspond to the physical Roper resonance. The double-pole structure of the Roper resonance was also observed in previous studies [25, 26]. Meson-baryon

---

\*Current address: Thomas Jefferson National Accelerator Facility, Newport News, Virginia 23606

†Current address: CEA, Centre de Saclay, Irfu/Service de Physique Nucléaire, 91191 Gif-sur-Yvette, France

‡Current address: Institut de Physique Nucléaire ORSAY, Orsay, France

§Current address: INFN, Sezione di Genova, 16146 Genova, Italy

¶Current address: Università di Roma Tor Vergata, 00133 Rome Italy

dressing should be taken into consideration in the interpretation of resonance electrocouplings as well as for the excited nucleon spectrum.

Our studies of resonance electrocouplings at small photon virtualities presented in this paper offer valuable information to further explore the role of meson-baryon and quark components in the  $N^*$  structure. The separation between the meson-baryon cloud and quark core contributions within a well-defined theoretical framework [27] can help pin down the domain of photon virtualities where quark components are the main contributor to the  $N^*$  structure. This kinematic domain is of particular interest for the studies of hadrons from the first principles of QCD, including Lattice QCD (LQCD) [28–35] and Dyson-Schwinger equation studies of QCD (DSEQCD) [35–41].

The CLAS detector at Jefferson Lab is a unique large-acceptance instrument designed for the comprehensive exploration of exclusive meson electroproduction. It offers excellent opportunities of studying the electroexcitation of nucleon resonances in detail and with precision. The CLAS detector has provided the dominant portion of all data on meson electroproduction in the resonance excitation region.

A variety of measurements of single pion electroproduction off protons, including polarization measurements, have been performed at CLAS in a range of  $Q^2$  from 0.16 to 6 GeV<sup>2</sup> [42]. The electroexcitation amplitudes for the low-lying resonances  $P_{33}(1232)$ ,  $P_{11}(1440)$ ,  $D_{13}(1520)$ , and  $S_{11}(1535)$  were determined over a wide range of  $Q^2$  in a comprehensive analysis of JLab-CLAS data on differential cross sections, longitudinally polarized beam asymmetries, and longitudinal target and beam-target asymmetries [15].

The combination of the large-acceptance CLAS detector and the continuous electron beam from CEBAF made it possible to measure  $\pi^+\pi^-p$  electroproduction cross sections with nearly full kinematic coverage for this three-body final hadron state [6, 43]. These are the most extensive data sets on unpolarized  $\pi^+\pi^-p$  electroproduction cross sections obtained so far. These data allowed for the first time the projection of nine one-dimensional differential cross sections, each sensitive to a different combination of resonance and background strength. The data of [6] were collected in the mass range  $1.31 \text{ GeV} < W < 1.56 \text{ GeV}$  and with photon virtualities  $0.25 \text{ GeV}^2 < Q^2 < 0.6 \text{ GeV}^2$ . A good description of these data was achieved within the framework of a phenomenological Jefferson Laboratory - Moscow State University (JM) reaction model [7], that allowed us to establish the mechanisms contributing to this exclusive reaction. The presence and strength of the contributing  $\pi^+\pi^-p$  electroproduction mechanisms were established by studying their kinematical dependencies and correlations in different one-fold differential cross sections.

In this work we present results on the electroexcitation of the  $P_{11}(1440)$  and  $D_{13}(1520)$  states, obtained from the analysis of data on  $\pi^+\pi^-p$  electroproduction off pro-

tons [6]. The analysis was carried out employing the JM reaction model [7], which was further developed to provide a framework for the determination of  $\gamma_v p N^*$  electrocouplings from a combined fit of unpolarized differential cross sections. In the previous studies [7] we did not attempt to isolate the contributions from resonances. In the analysis reported in this paper, we employ the JM model with the goal of isolating the resonant contributions for the individual differential cross sections. For the description of resonant amplitudes, we updated the Breit-Wigner (BW) parametrization, making it consistent with the restrictions required by the general unitarity condition. The reliable evaluation of the resonant contributions enabled for the first time the determination of the  $\gamma_v p N^*$  electrocouplings for the  $P_{11}(1440)$  and  $D_{13}(1520)$  states from charged double pion electroproduction off protons. This complements the results from  $N\pi$  electroproduction in an independent channel.

Analyses of different exclusive channels are essential for a reliable extraction of resonance parameters. Currently the separation of resonant and non-resonant parts of the electro production amplitudes can be done only within phenomenological reaction models. Therefore, the resonance parameters extracted from the meson electro production data fit may be affected by the model assumptions, and their credibility should be further examined. Non-resonant mechanisms in various meson-electroproduction channels are completely different, while the  $\gamma_v N N^*$  electrocouplings are the same. Independent analyses of different exclusive channels make it possible to test whether they give consistent results for the resonance electrocouplings. Most nucleon resonances decay into both  $N\pi$  and  $N\pi\pi$  final states. Studies of resonance electroexcitations in these channels with completely different non-resonant contributions offer independent information on  $N^*$  electrocouplings. Therefore, a successful description of the data on  $\pi^+n$ ,  $\pi^0p$ , and  $\pi^+\pi^-p$  electroproduction off protons with consistent  $N^*$  electrocoupling values provides clear evidence for the reliable extraction of these quantities from meson-electroproduction data.

Studies of the  $P_{11}(1440)$  resonance in  $\pi^+\pi^-p$  electroproduction off protons offer the additional opportunities to improve the knowledge on electrocouplings of this  $\approx 300 \text{ MeV}$  broad state. Contrary to  $N\pi$  electroproduction channels, the  $P_{33}(1232)$  resonance does not directly contribute to the resonant parts of the  $\pi^+\pi^-p$  electroproduction amplitude. Hence, the influence of the  $P_{33}(1232)$  resonance on the extracted electrocouplings of the  $P_{11}(1440)$  is much weaker.

The requirement of  $Q^2$ -independent  $N^*$  hadronic decay amplitudes in  $\pi^+\pi^-p$  electroproduction provides constraints on the  $N\pi\pi$  partial decay widths. This makes possible access to the  $\pi\Delta$  and  $\rho p$  partial hadronic decay widths of the  $P_{11}(1440)$  and  $D_{13}(1520)$  in the measurements of  $\pi^+\pi^-p$  electroproduction off protons.

## II. PHENOMENOLOGICAL MODEL JM FOR EVALUATION OF $\gamma_v p N^*$ ELECTROCOUPLINGS

The phenomenological meson-baryon model JM was developed to describe  $\pi^+\pi^-p$  electroproduction off protons [7, 44–48] with the primary objective of determining the resonance  $\gamma_v p N^*$  electrocouplings and the  $\pi\Delta$  and  $\rho p$  partial hadronic decay widths from a combined fit to all measured observables. In our current analysis of the CLAS  $\pi^+\pi^-p$  electroproduction data [6] the JM model was used to separate the resonant and non-resonant contributions to differential cross sections and to access the electrocouplings and  $\pi\Delta$ ,  $\rho p$  decay widths of the  $P_{11}(1440)$  and  $D_{13}(1520)$  resonances. Here we briefly discuss the basic ingredients of the JM model that are relevant to the objectives of this paper.

### A. Kinematics and cross sections

At a given invariant mass  $W$  and photon virtuality  $Q^2$ , the  $\gamma_v p \rightarrow \pi^+\pi^-p$  reaction can be fully described as

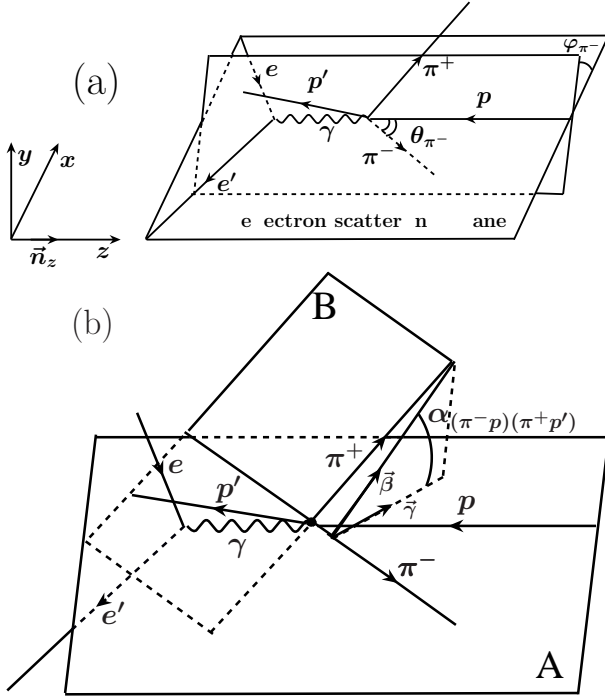


FIG. 1: Kinematic variables for the description of  $ep \rightarrow e'p'\pi^+\pi^-$  in the CM frame of the final-state hadrons corresponding to the first assignment presented in Section II A. Panel (a) shows the  $\pi^-$  spherical angles  $\theta_{\pi^-}$  and  $\varphi_{\pi^-}$ . Panel (b) shows the angle  $\alpha_{[p\pi^-][p'\pi^+]}$  between the two planes: one of them (plane A) is defined by the 3-momenta of the initial proton and the final  $\pi^-$ , the other (plane B) is defined by the 3-momenta of the two others final hadrons  $\pi^+$  and proton. The unit vectors  $\vec{\gamma}$  and  $\vec{\beta}$  are normal to the  $\pi^-$  three-momentum in the planes A and B, respectively.

a five-fold differential cross section  $d^5\sigma/d^5\tau$ , where  $d^5\tau$  is the phase-space volume of the five independent variables in the center-of-mass (CM) system of the final  $\pi^+\pi^-p$  state. There are many possible choices [49] of the five independent variables. After defining  $M_{\pi^+p}$ ,  $M_{\pi^-p}$ , and  $M_{\pi^+\pi^-}$  as invariant mass variables of the three possible two-particle pairs in the  $\pi^+\pi^-p$  system, we adopt the following three assignments:

1.  $d^5\tau_1 = dM_{p\pi^+}dM_{\pi^+\pi^-}d\Omega_{\pi^-}d\alpha_{[p'\pi^+][p\pi^-]}$ , where  $\Omega_{\pi^-}$  ( $\theta_{\pi^-}$ ,  $\varphi_{\pi^-}$ ) are the final  $\pi^-$  spherical angles with respect to the direction of the virtual photon, and  $\alpha_{[p'\pi^+][p\pi^-]}$  is the angle between Plane B defined by the momenta of the final  $p'\pi^+$  pair and Plane A defined by the momenta of the initial proton and the final  $\pi^-$ ;
2.  $d^5\tau_2 = dM_{p\pi^+}dM_{\pi^+\pi^-}d\Omega_{p'}d\alpha_{[\pi^+\pi^-][p'p]}$ , where  $\Omega_{p'}$  ( $\theta_{p'}$ ,  $\varphi_{p'}$ ) are the final proton spherical angles with respect to the direction of the virtual photon, and  $\alpha_{[\pi^+\pi^-][p'p]}$  is the angle between Plane B' defined by the momenta of the  $\pi^+\pi^-$  pair and Plane A defined by the momenta of the initial and final protons;
3.  $d^5\tau_3 = dM_{p\pi^+}dM_{p\pi^-}d\Omega_{\pi^+}d\alpha_{[p'\pi^-][p\pi^+]}$ , where  $\Omega_{\pi^+}$  ( $\theta_{\pi^+}$ ,  $\varphi_{\pi^+}$ ) are the final  $\pi^+$  spherical angles with respect to the direction of virtual photon, and  $\alpha_{[p'\pi^-][p\pi^+]}$  is the angle between Plane B'' defined by the momenta of the final  $p'\pi^-$  pair and Plane A'' defined by the momenta of the initial proton and the  $\pi^+$ .

All frame-dependent variables are defined in the final hadron center-of-mass (CM) frame.

The emission angles for the final state particles in the case of the first assignment are shown in Fig. 1. This choice is most suitable for describing  $\pi^+\pi^-p$  electroproduction through the  $\pi^-\Delta^{++}$  intermediate state, which is the dominant contributor of all isobar channels in the kinematic region covered by the data [6]. For the other assignments the emission angles of the final hadrons are analogous to the ones given in Fig. 1. The relations between the momenta of the final-state hadrons and the five variables of the first assignment can be found in the Ref. [6].

The  $\pi^+\pi^-p$  electroproduction data have been collected in the bins of a seven dimensional space. As mentioned above, five variables are needed to fully describe the final hadron kinematics, while to describe the initial state kinematics two others variables  $W$  and  $Q^2$  are required. The huge number of seven dimensional bins over the reaction phase space ( $\approx 100,000$  bins) does not allow us to use the correlated multi-fold differential cross sections in the analysis of electroproduction processes, where the statistics decrease drastically with the photon virtualities  $Q^2$ . More than half of the five-dimensional phase-space bins of the final hadrons is not populated due to statistical limitations. This is a serious obstacle for any analysis method that employs information on the behavior



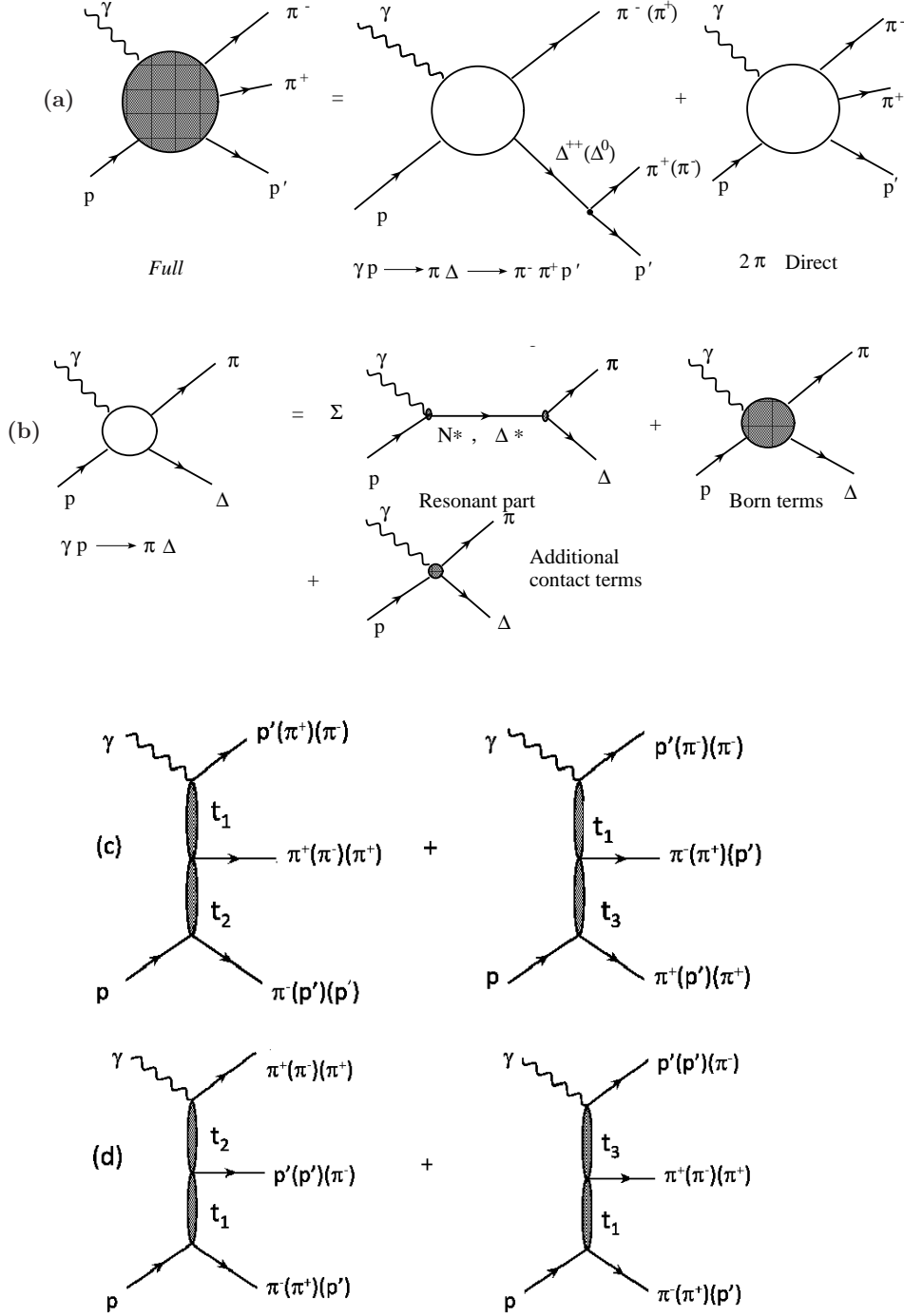


FIG. 2: Reaction mechanisms of the JM model [7] that contribute to  $\pi^+ \pi^- p$  electroproduction in the kinematic region covered by recent CLAS measurements [6] with  $W < 1.6$  GeV and  $0.25 \text{ GeV}^2 < Q^2 < 0.6 \text{ GeV}^2$ : 3-body mechanisms (a),  $\pi\Delta$  isobar channels (b), and direct  $2\pi$  production mechanisms that correspond to different assignments for the final state hadrons (c,d). The  $t_i$  ( $i=1,\dots,3$ ) stand for the squared transferred momenta in the exchange processes by unspecified particle(s), as described in [7] and shown by blobs in the (c) and (d) panels.

of multi-fold differential cross sections. We therefore use the following one-fold differential cross sections in each bin of  $W$  and  $Q^2$  covered by the measurements:

- invariant mass distributions for three pairs of the final particles  $d\sigma/dM_{\pi^+\pi^-}$ ,  $d\sigma/dM_{\pi^+p}$ , and

$$d\sigma/dM_{\pi^-p};$$

- angular distributions for spherical angles of the three final particles  $d\sigma/d(-\cos\theta_{\pi^-})$ ,  $d\sigma/d(-\cos\theta_{\pi^+})$ , and  $d\sigma/d(-\cos\theta_{p'})$  in the CM

frame;

- angular distributions for the three  $\alpha$ -angles described above and determined in the CM frame  $d\sigma/d\alpha_{[p'\pi^+][p\pi^-]}$ ,  $d\sigma/d\alpha_{[p'\pi^-][p\pi^+]}$ , and  $d\sigma/d\alpha_{[\pi^+\pi^-][pp']}$ .

The one-fold differential cross sections were obtained from integrating the five-fold differential cross sections over the relevant four others kinematic variables of  $d^5\tau_i$ . All details related to the evaluation of the  $\pi^+\pi^-p$  one-fold differential cross sections we are using for the extraction of resonance parameters can be found in Ref. [6].

## B. Relevant electroproduction mechanisms

The major part of the  $\pi^+\pi^-p$  electroproduction off protons at  $W < 1.6$  GeV is due to contributions from the two  $\pi\Delta$  isobar channels  $\pi^-\Delta^{++}$  and  $\pi^+\Delta^0$ . The  $\Delta^{++}(1232)$  resonance is clearly seen in all  $\pi^+p$  mass distributions for  $W > 1.4$  GeV, while contributions from the  $\pi^+\Delta^0$  isobar channel are needed to better describe the data in the low mass regions of the  $\pi^-p$  mass distributions. The observed in the data [6] strength of the  $\pi^-\Delta^{++}$  isobar channel is approximately nine times larger than that of  $\pi^+\Delta^0$  [7] due to isospin invariance. The contributions from all other isobar channels  $p\rho$ ,  $\pi^+D_{13}^0(1520)$ ,  $\pi^+F_{15}^0(1685)$ , and  $\pi^-P_{33}^{++}(1640)$ , which are incorporated into the JM-model [45–48] in order to describe the data at  $W > 1.6$  GeV, are negligible in the kinematic region covered in this analysis, and are not included in this work.

The production amplitudes relevant for our analysis of  $\gamma vp \rightarrow \pi^+\pi^-p$  are illustrated in Fig. 2. They consist of the  $\pi^-\Delta^{++}$  and  $\pi^+\Delta^0$  isobar channels and direct double pion production mechanisms. The production amplitudes for  $\pi\Delta$  intermediate states (Fig. 2b) consist of the resonant contributions  $\gamma_v N \rightarrow N^*, \Delta^* \rightarrow \pi\Delta$  and non-resonant terms. All resonances listed in Table I are included in the JM model. However, in the kinematic area covered in our measurements, only the  $P_{11}(1440)$ ,  $D_{13}(1520)$ , and  $S_{11}(1535)$  nucleon resonances have strength that is sufficient to manifest themselves in the one-fold differential cross-sections. Non-resonant amplitudes, depicted in the diagrams in Fig. 2b are computed from the well-established Born terms presented in Appendix A of Ref. [7]. The additional contact terms are implemented in the full  $\pi\Delta$  production amplitudes. They describe effectively the contributions from mechanisms other than the Born terms to  $\pi\Delta$  production and the part of the  $\pi\Delta$  final-state interactions (FSIs) that are not included in the JM model's absorptive approximation for FSIs [7, 50]. The Lorentz structure of these additional contact terms is determined by superposition of the two second-rank Lorentz tensors

$$\gamma^\mu p_\nu^\pi, \quad p_c^\delta \gamma^\delta g_{\mu\nu}, \quad (1)$$

$N^*$ states incorporated into the data fit	Mass, (GeV)	Total decay width $\Gamma_{tot}$ , (GeV)	Branching ratio $\pi\Delta$ , %	Branching ratio $\rho p$ , %	$N^*$ electro coupling variation in the fit
$P_{11}(1440)$	var	var	var	var	[57] var
$D_{13}(1520)$	var	var	var	var	[57] var
$S_{11}(1535)$	var	var	var	var	[15] fix
$S_{31}(1620)$	1.62	0.16	60	16	[46, 47] var
$S_{11}(1650)$	1.65	0.15	2	3	[58] var
$F_{15}(1680)$	1.68	0.12	12	5.5	[46, 47] var
$D_{13}(1700)$	1.74	0.19	53	45	[46, 47] fix
$D_{33}(1700)$	1.70	0.26	89	2	[46, 47] fix

TABLE I: List of resonances invoked in the  $\pi^+\pi^-p$  fit and their parameters: total decay widths  $\Gamma_{tot}$  and branching fractions (BF) to  $\pi\Delta$  and  $\rho p$  final states. The quoted values for the hadronic parameters are taken from fits to the earlier CLAS  $\pi^+\pi^-p$  data [43] using the 2005 version of the JM model [46, 47]. The quantities labeled as *var* correspond to the variable parameters fit to the CLAS  $\pi^+\pi^-p$  data [6] within the framework of the current JM model version [7] employing the unitarized BW ansatz of Section II D for the resonant contributions. Start values for the resonance electrocouplings are taken from the references listed in the last column and extrapolated to the  $Q^2$  area covered by the CLAS experiment [6].

where  $p_c = (2p_\nu^\pi - q_\gamma)$  is the difference of the final pion four-momentum  $p_\nu^\pi$  and the momentum transferred,  $q_\gamma - p_\nu^\pi$ . A parametrization of the additional contact-term amplitudes in the  $\pi\Delta$  channels may be found in Appendix B of Ref. [7].

All isobar channels combined account for 70% to 90% of the charged double-pion fully integrated cross sections in the kinematic region covered by data [6]. The remaining part of the cross sections comes from direct charged pion ( $2\pi$ ) production mechanisms, in which the  $\pi^+\pi^-p$  final state is created without the formation of unstable hadrons in the intermediate states. The presence of these mechanisms is required by the unitarity of the three-body  $\pi^+\pi^-p$  production amplitudes [51]. Their manifestation in  $\pi^+\pi^-p$  electroproduction was observed for the first time in our previous analyses of CLAS data [7, 47]. The dynamics of these processes was unknown and has been established from the CLAS data analysis within the framework of the JM model. The direct  $2\pi$ -production mechanisms incorporated in the JM model are depicted in Fig. 2(c,d). They represent two subsequent exchanges of unspecified particles, parametrized by propagators that depend exponentially on the running four-momenta squared. Each set of diagrams in Fig. 2 corresponds to various assignments of the final-state hadrons, resulting in different four-momenta squared running over propagators in the exchange amplitudes. The JM model extends for the first time the description of  $\pi^+\pi^-p$  electroproduction beyond the approximation of superimposed isobar channels by incorporating direct  $2\pi$ -production. Explicit expressions for the above-mentioned direct  $2\pi$ -

production amplitudes can be found in Appendices A-C of Ref. [7].

The relationships between  $\pi^+\pi^-p$  electroproduction cross sections and the three-body production amplitudes employed in the JM model are given in Appendix D of Ref. [7]. This information is required in order to compare the amplitudes of the JM model with the results from any other study of  $\pi^+\pi^-p$  electroproduction amplitudes.

### C. Breit-Wigner parametrization of resonant amplitudes

We start from a non-unitarized relativistic Breit-Wigner (BW) ansatz to describe the resonant contribution  $\langle\lambda_f|T_r|\lambda_\gamma\lambda_p\rangle$  in the helicity representation:

$$\langle\lambda_f|T_r|\lambda_\gamma\lambda_p\rangle = \sum_{N^*} \frac{\langle\lambda_f|T_{dec}|\lambda_R\rangle\langle\lambda_R|T_{em}|\lambda_\gamma\lambda_p\rangle}{M_r^2 - W^2 - i\Gamma_r(W)M_r}, \quad (2)$$

where  $M_r$  and  $\Gamma_r$  are the resonance mass and energy-dependent total width, respectively. The matrix elements  $\langle\lambda_R|T_{em}|\lambda_\gamma\lambda_p\rangle$  and  $\langle\lambda_f|T_{dec}|\lambda_R\rangle$  are the electromagnetic production and hadronic decay amplitudes of the  $N^*$  with helicity  $\lambda_R = \lambda_\gamma - \lambda_p$ , in which  $\lambda_\gamma$  and  $\lambda_p$  stand for the helicities of the photon and proton in the initial state, and  $\lambda_f$  represents the helicities of final-state hadrons in the  $N^*$  decays.

The hadronic decay amplitudes  $\langle\lambda_f|T_{dec}|\lambda_R\rangle$  are related to the  $\Gamma_{\lambda_f}(W)$  partial hadronic decay widths of the  $N^*$  to  $\pi\Delta$  or  $\rho p$  final states  $f$  of helicity  $\lambda_f$  by:

$$\langle\lambda_f|T_{dec}|\lambda_R\rangle = \langle\lambda_f|T_{dec}^{J_r}|\lambda_R\rangle d_{\mu\nu}^{J_r}(\cos\theta^*) e^{i\mu\phi^*},$$

with  $\mu = \lambda_R$  and  $\nu = -\lambda_\Delta$  for the  $\pi\Delta$  intermediate state and  $\nu = \lambda_{p'} - \lambda_\rho$  for the  $\rho p'$  intermediate state, and

$$\langle\lambda_f|T_{dec}^{J_r}|\lambda_R\rangle = \frac{2\sqrt{2\pi}\sqrt{2J_r+1}M_r\sqrt{\Gamma_{\lambda_f}}}{\sqrt{\langle p_i^r \rangle}} \sqrt{\frac{\langle p_i^r \rangle}{\langle p_i \rangle}}. \quad (3)$$

The means  $\langle p_i^r \rangle$  and  $\langle p_i \rangle$  are the magnitudes of the three-momenta of the final  $\pi$  for the  $N^* \rightarrow \pi\Delta$  decay ( $i=1$ ) or of the final proton for the  $N^* \rightarrow \rho p$  decay ( $i=2$ ), evaluated at  $W = M_r$  and at the running  $W$ , respectively, and averaged over the running mass of the unstable hadron in the intermediate state. The variables  $\theta^*$ ,  $\phi^*$  are the CM polar and azimuthal angles for the final  $\pi$  ( $N^* \rightarrow \pi\Delta$  decay) or the final proton ( $N^* \rightarrow \rho p$  decay). The symbol  $J_r$  stands for the  $N^*$  spin. This relationship between the  $N^*$  hadronic decay amplitudes and the partial decay widths was derived for the  $N^* \rightarrow \pi\Delta$  decay in our previous article [50]. All details on the parametrization of the resonance hadronic decay amplitudes in the JM model can be found in Appendix A of this paper.

Energy dependencies of the partial hadronic decay widths are described under the assumption that centrifugal barrier-penetration factors are the major contributors

to the off-shell behavior of resonance hadronic decay amplitudes [50, 52]:

$$\sqrt{\Gamma_{LS}} = \sqrt{\Gamma_{LS}^r} \cdot \left[ \frac{M_r (J_l^2(p^r R) + N_l^2(p^r R))}{W (J_l^2(pR) + N_l^2(pR))} \right]^{1/2}, \quad (4)$$

where  $J_l$  and  $N_l$  are the Bessel and Neumann functions. The factor in square brackets represent the ratio of barrier penetration factors for the final meson with orbital angular momentum  $l$  evaluated at  $W = M_r$  and at the running  $W$ . The variable  $R$  represents the interaction radius whose value was set to 1 fm, and  $\sqrt{\Gamma_{LS}^r}$  stands for the decay amplitude estimated at the resonant point. The partial decay amplitudes  $\sqrt{\Gamma_{LS}}$  of Eq. (4) are transformed from the  $LS$  to the helicity representation  $\sqrt{\Gamma_{\lambda_f}}$  (see the Appendix A) and used to compute the  $N^*$  hadronic decay amplitudes via Eq. (3).

In the JM model, the  $N^*$  total decay width  $\Gamma_r(W)$  in Eq. (2) is evaluated as a sum over all partial decay widths. In this way we ensure unitarity of the resonant amplitude for a single resonance contribution. The unitarization procedure in the actual case of many contributing resonances will be discussed in Section IID.

The resonance electroexcitation amplitudes  $\langle\lambda_R|T_{em}|\lambda_\gamma\lambda_p\rangle$  in Eq. (2) are related to the  $\gamma_v NN^*$  electrocouplings  $A_{1/2}$ ,  $A_{3/2}$ , and  $S_{1/2}$  for nucleons. The definition of these electrocouplings in the JM model is consistent with the Review of Particle Physics (RPP) [53] relation between the  $A_{1/2}$ ,  $A_{3/2}$  electrocouplings and the  $N^*$  electromagnetic decay width  $\Gamma_\gamma$ :

$$\Gamma_\gamma = \frac{q_{\gamma,r}^2}{\pi} \frac{2M_N}{(2J_r+1)M_r} \left[ |A_{1/2}|^2 + |A_{3/2}|^2 \right], \quad (5)$$

where  $q_{\gamma,r}$  is the three-momentum modulus of the photon at  $W = M_r$  in the CM frame. The transition amplitudes  $\langle\lambda_R|T_{em}|\lambda_\gamma\lambda_p\rangle$  are related to the  $\gamma_v NN^*$   $A_{1/2}$ ,  $A_{3/2}$ , and  $S_{1/2}$  electrocouplings by imposing the requirement that the BW parametrization [54] of the resonant cross section for a single contributing resonance should be reproduced:

$$\sigma(W) = \frac{\pi}{q_\gamma^2} (2J_r+1) \frac{M_r^2 \Gamma_i(W) \Gamma_\gamma}{(M_r^2 - W^2)^2 - M_r^2 \Gamma_r^2(W)} \frac{q_\gamma}{K}. \quad (6)$$

Here the photon equivalent energy  $K = \frac{W^2 - M_N^2}{2W}$ ,  $q_\gamma$  is the absolute value of the initial photon three-momentum of virtuality  $Q^2 > 0$   $q_\gamma = \sqrt{Q^2 + E_\gamma^2}$  and the energy  $E_\gamma$  in the CM frame at the running  $W$

$$E_\gamma = \frac{W^2 - Q^2 - M_N^2}{2W}. \quad (7)$$

The  $q_{\gamma,r}$  value in Eq. (5) can be computed from Eq. (7) at  $W=M_r$ .  $\Gamma_i(W)$  is the energy-dependent hadronic decay width to the final state  $\pi\Delta$  ( $i=1$ ) or  $\rho p$  ( $i=2$ ). The factor  $\frac{q_\gamma}{K}$  in Eq. (6) is equal to unity at the photon point. It accounts for the choice [6] of the virtual

photon flux in the evaluation of the virtual photon cross sections. In this way we obtain the following relationship between the transition amplitudes  $\langle \lambda_R | T_{em} | \lambda_\gamma \lambda_p \rangle$  and the  $\gamma_v NN^*$  electrocouplings:

$$\begin{aligned} \langle \lambda_R | T_{em} | \lambda_\gamma \lambda_p \rangle &= \frac{W}{M_r} \sqrt{\frac{8M_N M_r q_{\gamma_r}}{4\pi\alpha}} \sqrt{\frac{q_{\gamma_r}}{q_\gamma}} A_{1/2,3/2}(Q^2), \\ \text{with } |\lambda_\gamma - \lambda_p| &= \frac{1}{2}, \frac{3}{2} \text{ for transverse photons, and} \\ \langle \lambda_R | T_{em} | \lambda_\gamma \lambda_p \rangle &= \frac{W}{M_r} \sqrt{\frac{16M_N M_r q_{\gamma_r}}{4\pi\alpha}} \sqrt{\frac{q_{\gamma_r}}{q_\gamma}} S_{1/2}(Q^2), \\ &\text{for longitudinal photons.} \end{aligned} \quad (8)$$

The factor  $4\pi\alpha$  in Eqs. (8) reflects the particular relationship between the JM model amplitudes and cross sections [7], when the absolute value of the electron charge is factorized out of the production amplitudes.

#### D. Unitarization of the full resonant amplitudes

The BW ansatz, described in Section II C, provides unitary contributions from any individual  $N^*$  state to the resonant part of the electroproduction amplitudes. However, the full resonant amplitude, which represents a superposition of contributions from all  $N^*$  states, is not unitary. Figure 3 schematizes the processes that contribute to the resonant propagator dressing. They consist of transitions between the same and different  $N^*$  states mediated by the strong interaction. The regular BW ansatz incorporates only transitions between the same  $N^*$  states shown by the blob in the top panel of Fig. 3. The unitarization is achieved via inclusion of both diagrams in Fig. 3, allowing us to take into account transitions between both the same and different  $N^*$  states (bottom panel in Fig. 3) in the dressed resonant propagators. We replaced the usual BW ansatz by its unitarized extension originally proposed in Ref. [55]. This ansatz was adjusted for the description of the BW resonance electroproduction amplitudes of Eq. (2) employed in the JM model. The full resonant amplitude of the unitarized extension of the BW ansatz satisfies the unitarity condition [55].

Unitarized resonance amplitudes in the JM model incorporate photo- and electro-excitation amplitudes of all relevant resonances  $\alpha$ , all possible transitions between the initial  $N^*$  state  $\alpha$  and the final  $N^*$  state  $\beta$ , and hadronic decays of  $\beta$ . Fully unitarized resonance amplitudes are determined by the sum of the products of the electromagnetic excitation amplitudes of the  $\alpha$ -th  $N^*$  state  $\langle \lambda_\alpha | T_{em} | \lambda_\gamma \lambda_p \rangle$ , the hadronic decay amplitudes of the  $\beta$ -th  $N^*$  state  $\langle \lambda_f | T_{dec} | \lambda_\beta \rangle$ , the dressed propagator

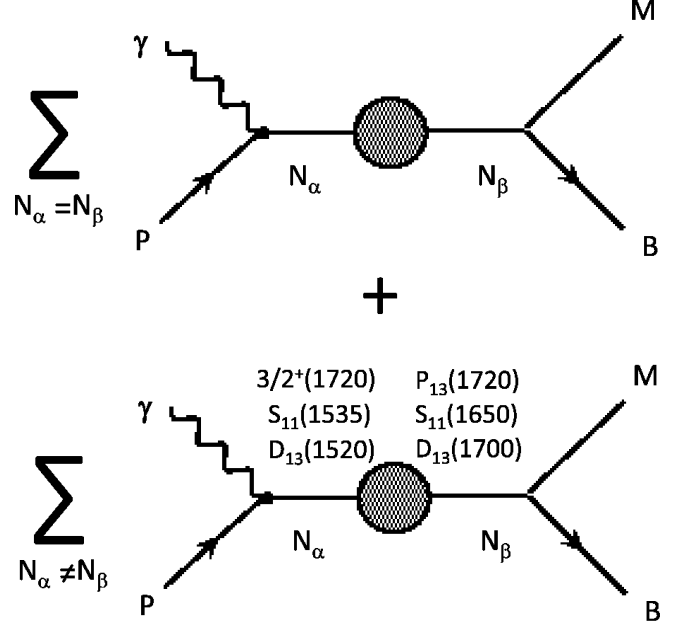


FIG. 3: Diagrams showing the unitarized BW ansatz of the JM model, which incorporates transitions via the dressed resonance propagator between states listed in Table I for the same  $N_\alpha = N_\beta$  (top) and different  $N_\alpha \neq N_\beta$  resonances as allowed by the conservation laws of the strong interaction (bottom).

$S_{\alpha\beta}$ , and

$$\langle \lambda_f | T_{res} | \lambda_\gamma \lambda_p \rangle = \sum_{\alpha, \beta} \langle \lambda_f | T_{dec} | \lambda_\beta \rangle S_{\alpha\beta} \langle \lambda_\alpha | T_{em} | \lambda_\gamma \lambda_p \rangle. \quad (9)$$

The sum incorporates all transitions between the  $\alpha$ -th initial and the  $\beta$ -th final  $N^*$  states that are allowed by quantum number conservation laws. It runs over all repeated indices  $\alpha$  and  $\beta$  that label the  $N^*$  states. As a consequence of angular momentum conservation  $\lambda_\alpha = \lambda_\beta$ , but these two helicities stand either for the same  $N^*$  states if  $\alpha = \beta$  (diagonal transitions) or different  $N^*$  states if  $\alpha \neq \beta$  (off-diagonal transitions). The index  $f$  represents the final-state helicities, either for  $\pi\Delta$  or for  $\rho p$ .

The expression for the inverse dressed propagator  $S_{\alpha\beta}^{-1}$  is obtained in Ref. [55] (see Eq. (6) in Ref. [55]). However, the parametrization of the  $N^*$  propagator in Ref. [55] and in JM are different. Therefore, we change the inverse resonant propagator  $S_{\alpha\beta}^{-1}$  of Ref. [55], so that it coincides with the single  $N^*$  contribution employed in the JM model. In this way we obtain

$$S_{\alpha\beta}^{-1} = M_{N^*}^2 \delta_{\alpha\beta} - i \left( \sum_k \sqrt{\Gamma_{\alpha k} \Gamma_{\beta k}} \right) \sqrt{M_{N_\alpha^*} M_{N_\beta^*}} - W^2 \delta_{\alpha\beta}, \quad (10)$$

where the index  $k$  represents the partial  $N^*$  hadronic decay widths to all possible final states, decomposed over



$LS$  partial waves. For a single  $N^*$  contribution, Eq. (10) coincides with the inverse BW propagator in Eq. (2).

The resonant contribution at  $W < 1.6$  GeV incorporates the  $N^*$  states listed in Table I and the  $3/2^+(1720)$  candidate state observed in the previous analysis of the CLAS  $\pi^+\pi^-p$  electroproduction data [43]. The conservation laws in strong interactions allow transitions in dressed resonant propagators only between the following pairs of  $N^*$  states:  $D_{13}(1520)$  and  $D_{13}(1700)$ ,  $S_{11}(1535)$  and  $S_{11}(1650)$ , and  $3/2^+(1720)$  candidate and  $P_{13}(1720)$  (bottom panel in Fig. 3). Therefore, the unitarized resonant amplitude represents the sum of regular BW amplitudes over all other  $N^*$  states with only diagonal transitions in the dressed resonance propagators plus contributions from the aforementioned pairs of  $N^*$  states that have both diagonal and non-diagonal transitions in the resonant propagators. The contributions from each pair of  $N^*$  states  $\langle \lambda_f | T_{2res} | \lambda_\gamma \lambda_p \rangle$  are determined by Eq. (9) with indices  $\alpha$  and  $\beta$  running from 1 to 2, resulting in  $2 \times 2$   $S_{\alpha\beta}^{-1}$  matrices. After inversion of  $S_{\alpha\beta}^{-1}$  in Eq. (10) and insertion into Eq. (9), we get the following expressions for the contribution from each of the three pairs of  $N^*$  states listed in Fig. 3:

$$\begin{aligned} \langle \lambda_f | T_{2res} | \lambda_\gamma \lambda_p \rangle &= \frac{1}{\det[S_{\alpha\beta}^{-1}]}^* \\ &\{ \langle \lambda_f | T_{dec} | \lambda_1 \rangle (M_2^2 - i\Gamma_2(W)M_2 - W^2) \langle \lambda_1 | T_{em} | \lambda_\gamma \lambda_p \rangle \\ &+ \langle \lambda_f | T_{dec} | \lambda_2 \rangle (M_1^2 - i\Gamma_1(W)M_1 - W^2) \langle \lambda_2 | T_{em} | \lambda_\gamma \lambda_p \rangle \\ &+ i \langle \lambda_f | T_{dec} | \lambda_2 \rangle \sum_k \sqrt{\Gamma_{1k}\Gamma_{2k}} \sqrt{M_{N_1^*}M_{N_2^*}} \langle \lambda_1 | T_{em} | \lambda_\gamma \lambda_p \rangle \\ &+ i \langle \lambda_f | T_{dec} | \lambda_1 \rangle \sum_k \sqrt{\Gamma_{1k}\Gamma_{2k}} \sqrt{M_{N_1^*}M_{N_2^*}} \langle \lambda_2 | T_{em} | \lambda_\gamma \lambda_p \rangle \}. \end{aligned} \quad (11)$$

The first two terms in Eq. (11) correspond to the diagonal  $S_{\alpha\beta}$  elements. They describe the processes depicted in the top panel of Fig. 3. The two other terms correspond to transition between different  $N^*$  states, shown in the bottom panel of Fig. 3. The determinant of  $S_{\alpha\beta}^{-1}$  can be computed from Eq. (10) as

$$\begin{aligned} \det[S_{\alpha\beta}^{-1}] &= (M_1^2 - i\Gamma_1(W)M_1 - W^2) \cdot \\ &(M_2^2 - i\Gamma_2(W)M_2 - W^2) + \left( \sum_k \sqrt{\Gamma_{1k}\Gamma_{2k}} \right)^2 M_1 M_2. \end{aligned} \quad (12)$$

It follows from Eqs. (11) and (12), that if transitions between two different  $N^*$  states in the dressed resonant propagators become impossible, then

$$\sum_k \sqrt{\Gamma_{1k}\Gamma_{2k}} = 0, \quad (13)$$

namely, all off-diagonal terms become zero, while the diagonal terms give rise to the amplitudes of the regular BW ansatz. When the transitions between the pairs of

$N^*$  states are turned on, they not only add off-diagonal terms to Eq. (11), but they also change the effective propagator in the  $\langle \lambda_f | T_{2res} | \lambda_\gamma \lambda_p \rangle$  amplitude with respect to the BW ansatz Eq. (2), determined by  $1/\det[S_{\alpha\beta}^{-1}]$ .

### III. THE CLAS DATA FIT

The resonance parameters obtained in this paper are fit to the CLAS  $\pi^+\pi^-p$  electroproduction differential cross sections [6]. A realistic evaluation of resonance electrocoupling uncertainties extracted in the fit is an important objective of our analysis. We require that the ranges of resonance electrocouplings extracted from the  $\pi^+\pi^-p$  electroproduction channel take into account both uncertainties in the measured differential cross sections and in the JM model parameters. In order to provide a realistic evaluation of resonance parameters, we abandoned the traditional least-squares fit, since the parameters extracted in such a fit correspond to a single presumed global minimum, while the experimental data description achieved with others local minima may be equally good within the data error bars. Furthermore, the traditional evaluation of fit-parameter uncertainties, based on the error propagation matrix, cannot be used for the same reason.

A special procedure was developed to obtain not only the best fit, but also to establish bands of computed cross sections that are compatible with the data within their uncertainties. In the fit we vary simultaneously non-resonant and resonant parameters of the JM model given in Tables I and II, respectively, around their start values, employing unrestricted normal distributions. The choice of the start parameters and the normal distribution  $\sigma$ -values employed for parameter variation will be further described below. For each trial set of the JM-model resonant and non-resonant parameters we compute nine measured one-fold differential  $\pi^+\pi^-p$  cross sections, and the  $\chi^2$  per data point values ( $\chi^2/d.p.$ ). The  $\chi^2/d.p.$  values were estimated in point-by-point comparisons between the measured and computed one-fold differential cross sections in all bins of  $W$  and  $Q^2$  covered by the CLAS  $\pi^+\pi^-p$  data of Ref. [6]. In the fit we selected computed one-fold differential cross sections closest to the data with  $\chi^2/d.p.$  less than a predetermined maximum value  $\chi_{max}^2/d.p.$ . The values of  $\chi_{max}^2/d.p.$  were obtained by requiring that the computed cross sections with smaller  $\chi^2/d.p.$  be within the data uncertainties for the majority of the data points, based on point-by-point comparisons between the measured and the computed cross sections (see examples in Figs. 4, 5). In this fit procedure we obtain the  $\chi^2/d.p.$  intervals within which the computed cross sections describe the data equally well within the data uncertainties.

The resonance parameters obtained from all these equally good fits are averaged and their mean values are taken as the resonance parameters extracted from the data. Dispersions in these parameters are taken as the

Variable parameters	Ranges covered in variations of the start parameters, % from their values
Magnitude of the additional contact term amplitude in the $\pi^-\Delta^{++}$ sub-channel	45.0
Magnitude of the additional contact term amplitude in the $\pi^+\Delta^0$ sub-channel	60.0
Magnitudes of six $2\pi$ direct production amplitudes	30.0

TABLE II: Variable parameters of non-resonant mechanisms incorporated into the JM model [7]. The ranges in the table correspond to the  $3\sigma$  areas around the start values of parameters.

$N^*$ states	Mass, (MeV)	Total decay width, $\Gamma_{tot}$ , (MeV)
$P_{11}(1440)$	1430-1480	200-450
$D_{13}(1520)$	1515-1530	100-150
$S_{11}(1535)$	1510-1560	100-200

TABLE III: Allowed  $N^*$  hadronic parameter variations in the fit of the CLAS  $\pi^+\pi^-p$  electroproduction data [6].

uncertainties. Our fitting procedure allows us to obtain more realistic uncertainties of the fit parameters than from the usual least-squares method. In this way we take into account both statistical uncertainties in the data and systematic uncertainties imposed by the use of the JM reaction model.

We vary the parameters of the JM model, listed in Table II for the non-resonant mechanisms, which are relevant in describing the CLAS  $\pi^+\pi^-p$  data [6]. They are limited to non-resonant  $\pi\Delta$  sub-channels and direct  $2\pi$ -electroproduction.

The magnitudes of the additional contact terms in the  $\pi^-\Delta^{++}$  and  $\pi^+\Delta^0$  isobar channels (row (b) in Fig. 2), as well as the magnitudes of all direct  $2\pi$ -production amplitudes (rows (c),(d) in Fig. 2), are chosen as variable parameters. All these parameters were determined in the fit to the CLAS data on  $\pi^+\pi^-p$  electroproduction in our previous analysis [7] without variation of the resonance parameters. In the CLAS data fit presented in this paper, the values of the aforementioned non-resonant parameters of the JM model are re-evaluated under simultaneous variation of:

- the magnitudes of additional contact-term amplitudes in the  $\pi^-\Delta^{++}$  and  $\pi^+\Delta^0$  isobar channels (2 parameters per  $Q^2$  bin);
- the magnitudes of all direct  $2\pi$ -production amplitudes (6 parameters per  $Q^2$  bin);
- the resonant parameters listed in Table I. The CLAS  $\pi^+\pi^-p$  data [6] are mostly sensitive to the

electrocouplings of the  $P_{11}(1440)$  and  $D_{13}(1520)$  states (5 resonance electrocouplings per  $Q^2$  bin), to the  $\pi\Delta$  and  $\rho p$  hadronic decay widths of these two resonances, and to the  $S_{11}(1535)$  state (6 parameters that remain the same in the entire  $Q^2$  area covered by the measurements).

Therefore, we consistently account for the correlations between variations of the non-resonant and the resonant contributions while extracting the resonant parameters.

The  $W$ -dependences of the magnitudes of the additional contact-term amplitudes in the  $\pi\Delta$  sub-channels and of the magnitudes of the direct  $2\pi$ -production amplitudes are adopted from our previous analysis [7]. We apply multiplicative factors to the magnitudes of the extra contact-term amplitudes and the  $2\pi$  direct-production amplitudes. The multiplicative factors are  $W$ -independent within any  $Q^2$ -bin, but they are fit to the data in each  $Q^2$ -bin independently. In this way we retain the smooth  $W$ -dependences of the non-resonant contributions established in our previous analysis [7].

We use two parameters for the variation of the magnitudes of additional contact-term amplitudes in the  $\pi^-\Delta^{++}$  and  $\pi^+\Delta^0$  isobar channels. However, the non-resonant parameters in the  $\pi^+\Delta^0$  isobar channel have a rather small impact on the fit, since the non-resonant contributions of the  $\pi^+\Delta^0$  isobar channel are approximately a factor 9 smaller than that of the  $\pi^-\Delta^{++}$ .

The parameters for the non-resonant Born terms in the  $\pi\Delta$  sub-channels ((b)-row in Fig. 2) include the  $p\pi\Delta$  coupling and cut-off for this hadron transition form factor, as well as the electromagnetic pion and nucleon form factors [50]. All these parameters are taken from previous studies of meson photo-, electro-, and hadroproduction referred to in Ref. [7] and are kept fixed for the current fit.

Different assignments of final hadrons in  $2\pi$ -direct production mechanisms, as shown in Fig. 2 (rows (c),(d)), result in 12 different sub-processes. Our previous analysis [7] demonstrated that the magnitudes of all these sub-processes are determined by six independent parameters. In the current fit we vary these six parameters of the direct  $2\pi$ -production amplitudes.

In the fitting procedure described above, nine one-fold  $\pi^+\pi^-p$  differential cross sections are computed with non-resonant variable parameters of the JM model obtained by employing unrestricted normal distributions around their start values with  $\sigma$ -parameters of 10%-20% of their start values (see Table II). In this way we explore mostly the range of  $\approx 3\sigma$  around the start parameter values. These ranges for non-resonant parameter variations in the JM model are shown in Table II as a percentage of their start values.

In this fit we also vary the  $\gamma_v p N^*$  electrocouplings and the  $\pi\Delta$  and  $\rho p$  hadronic partial decay widths of the  $P_{11}(1440)$  and  $D_{13}(1520)$  resonances around their start values. The start values of the  $P_{11}(1440)$  and  $D_{13}(1520)$  electrocouplings are determined by interpolating the results from the analysis [57] of the CLAS data on  $N\pi$  elec-

troproduction off protons into the range  $0.4 \text{ GeV}^2 < Q^2 < 0.6 \text{ GeV}^2$  and extrapolating these results into the  $Q^2$ -area from  $0.25 \text{ GeV}^2$  to  $0.4 \text{ GeV}^2$ . The electrocouplings of the  $P_{11}(1440)$  and  $D_{13}(1520)$  resonances are varied employing normal distributions with  $\sigma$  parameters equal to 30% of their start values. There are no restrictions on the minimum or maximum trial electrocoupling values. The normal distributions allow us to explore mostly the area of  $\approx 3\sigma$  around their start values or 90% around electrocoupling start values.

The  $\pi^+\pi^-p$  electroproduction channel has also some sensitivity to the  $S_{11}(1535)$  state, which couples dominantly to the  $N\pi$  and  $N\eta$  final states. The  $S_{11}(1535)$  electrocouplings were taken from the CLAS analysis of  $N\pi$  electroproduction [15] and varied strictly inside the uncertainties reported in that paper.

The  $\pi\Delta$  and  $\rho p$  hadronic decay widths of the  $P_{11}(1440)$ ,  $D_{13}(1520)$ , and  $S_{11}(1535)$  resonances are varied around their start values taken from previous analyses of the CLAS double pion electroproduction data [46–48] in ranges restricted by the total  $N^*$  decay widths and their uncertainties, as shown in Table III. The total  $N^*$  decay widths were obtained by summing the partial widths over all decay channels. Partial hadronic decay widths to all final states other than  $\pi\Delta$  and  $\rho p$  are computed as the products of RPP [53] values of  $N^*$  total decay widths and branching fractions for decays to particular hadronic final states, that are taken from analyses [56] of hadroproduction experiments. We varied the  $\pi\Delta$  and  $\rho p$  hadronic decay widths of the  $P_{11}(1440)$ ,  $D_{13}(1520)$ , and  $S_{11}(1535)$  resonances simultaneously with their masses, keeping the hadronic  $N^*$  parameters independent of  $Q^2$ . Accounting for the correlations of the  $N^*$  electromagnetic and hadronic decay parameters in a combined variation is important for a credible extraction of the resonance parameters and, in particular, for the evaluation of their uncertainties.

The here developed fit procedure allows us to determine the  $\pi\Delta$  and  $\rho p$  hadronic decay widths of the  $P_{11}(1440)$ ,  $D_{13}(1520)$ , and  $S_{11}(1535)$ . The resonance total decay widths are affected by the variation of their  $\pi\Delta$  and  $\rho p$  partial decay widths. Instead, when varying resonance electrocouplings, the  $N^*$  total decay widths of resonances are kept almost unchanged. Resonance hadronic decay amplitudes are independent of  $Q^2$ , while resonance electrocouplings represent the functional dependencies on the photon virtualities. These distinctive features allow us to disentangle resonance electromagnetic and hadronic decay amplitudes in the fit of the CLAS data [6] and to obtain the  $\pi\Delta$  and  $\rho p$  hadronic decay widths of the  $P_{11}(1440)$ ,  $D_{13}(1520)$ , and  $S_{11}(1535)$ .

To account for the contributions from the tails of higher mass resonances, electrocouplings of all  $N^*$  states marked in Table I as “var” are varied around their start values. For resonances with masses above 1.6 GeV, except the  $S_{11}(1650)$  state, the start values for electrocouplings are taken from the results of previous analyses [46, 47] of  $\pi^+\pi^-p$  electroproduction data [43] after the

$Q^2$ bins, (GeV <sup>2</sup> )	$W$ intervals, (GeV)	Number of fitted points	$\chi^2/d.p.$ intervals for selected cross sections
0.25-0.30	1.44-1.56	378	2.66-2.74
0.30-0.35	1.41-1.54	378	
0.35-0.40	1.41-1.54	378	
0.40-0.45	1.39-1.51	373	1.87-2.04
0.45-0.50	1.39-1.49	309	
0.50-0.55	1.39-1.51	360	1.57-1.75
0.55-0.60	1.34-1.44	279	

TABLE IV: Quality of the CLAS  $\pi^+\pi^-p$  fit within the framework of the JM model [7]. Horizontal lines separate the three  $Q^2$ -intervals, in which the fits were carried-out independently.

extrapolation into the  $Q^2$  range of the current analysis ( $0.25\text{--}0.6 \text{ GeV}^2$ ). The  $S_{11}(1650)$  state may have a more pronounced impact on the extraction of the  $P_{11}(1440)$  and  $D_{13}(1520)$  resonance parameters, since the  $S_{11}(1535)$  and  $S_{11}(1650)$  states are mixed in the dressed resonance propagator of the unitarized BW ansatz employed in the JM model. For this reason we prefer to have more accurate start values for the  $S_{11}(1650)$  electrocouplings. They are computed within the framework of the single quark transition model (SQTm) [58] from electrocouplings of the  $S_{11}(1535)$  state that are available from analyses of  $N\pi$  and  $N\eta$  electroproduction data [1]. Electrocouplings of the  $D_{13}(1700)$  and  $D_{33}(1700)$  resonances are kept fixed at their start values, since the masses of these resonances are far outside of the  $W$  area covered by the CLAS  $\pi^+\pi^-p$  electroproduction data [6]  $W < 1.6 \text{ GeV}$ .

The  $\pi\Delta$  and  $\rho p$  partial hadronic decay widths for  $N^*$  states other than the  $P_{11}(1440)$ ,  $D_{13}(1520)$ , and  $S_{11}(1535)$  resonances are taken from previous analyses of the CLAS double pion electroproduction data [46–48]. They are in a reasonable agreement with the values reported in the RPP [53]. The respective branching fractions are listed in Table I.

We fit the CLAS data [6] consisting of nine differential cross sections of the  $ep \rightarrow e'p'\pi^+\pi^-$  electroproduction reaction in all bins of  $W$  and  $Q^2$  in the kinematic region:  $1.35 \text{ GeV} < W < 1.57 \text{ GeV}$  and  $0.25 \text{ GeV}^2 < Q^2 < 0.6 \text{ GeV}^2$  within the framework of the fit procedure described above. Three intervals of  $Q^2$  separated in Table IV by horizontal solid lines are fit independently. The  $\chi^2/d.p.$  intervals, that correspond to equally good data description within the error bars are shown in Table IV. Their values demonstrate the quality of the CLAS  $\pi^+\pi^-p$  data description achieved in the fits. Examining the description of the nine one-fold differential cross sections, we found that the  $\chi^2/d.p.$  values are determined mostly by the random deviations of some experimental data points from the bunches of computed fit cross sections. There are no discrepancies in describing the shapes of the differential cross sections, which would manifest themselves systematically in neighboring bins of  $W$  and  $Q^2$ . Typical examples for  $W=1.51 \text{ GeV}$  and neighboring  $Q^2$  intervals

centered at 0.38 GeV<sup>2</sup> and 0.42 GeV<sup>2</sup> are shown in Fig. 4 and Fig. 5, respectively.

The sets of computed differential cross sections with  $\chi^2/d.p.$  values within the intervals given in the Table IV offer the best data descriptions achievable within the framework of the JM model. The minimal values of  $\chi^2/d.p.$  in each interval represent the global minima of these fits. We found that the increases of the  $\chi^2/d.p.$  values within the intervals listed in the Table IV change the computed differential cross sections, but still keep them inside the data uncertainties, offering equally good data descriptions in all these fits with different sets of JM model parameters. The mean values of the resonance parameters from these sets and their dispersions (statistical r.m.s.) are determining the resonance parameters and their uncertainties, as it was described at the beginning of this Section.

Since only statistical data uncertainties are used in the computation of the  $\chi^2/d.p.$  values listed in the Table IV, we concluded that a reasonable data description was achieved. The  $\chi^2/d.p.$  values of our fits are comparable with those obtained in the fit of the CLAS  $N\pi$  electroproduction data published in [15], as well as with those obtained in the MAID analysis [62].

#### IV. EVALUATION OF $\gamma_v p N^*$ ELECTROCOUPLINGS AND RESONANCE HADRONIC DECAY PARAMETERS

The extraction of resonance electrocouplings using the JM model relies on fitting resonant and non-resonant contributions to measured differential cross sections. Therefore, we first have to check the quality of the separation between resonant and non-resonant contributions achieved in the data fit.

##### A. Separation of resonant and non-resonant contributions to the $\pi^+\pi^-p$ cross sections

With the parameters determined from the fits, we now use the JM model to evaluate the contributions from resonant and non-resonant parts to the cross sections. This is done by computing the nine differential cross sections without the resonant parts and with only the resonant parts for all trial differential cross sections of the JM model selected in the fit. In this way we also determine the ranges of the resonant and non-resonant contributions to the cross sections as imposed by the uncertainties of the experimental data. These ranges account for the uncertainties of the non-resonant parameters listed in Table II and for all correlations between resonance and non-resonant amplitudes. Therefore, we obtain reliable estimates for the uncertainties of the resonant and non-resonant contributions to the differential cross sections. Examples of the separated resonant and non-resonant contributions for two particular  $W$  and  $Q^2$  bins are shown

in Figs. 4 and 5. The interference between the resonant and non-resonant amplitudes is clearly seen in all angular distributions. The differences between the fitted  $\pi^+\pi^-p$  differential cross sections and their non-resonant parts are larger than the resonant contributions for a majority of the data points in the angular distributions of the final hadrons, offering clear evidence for the interference between resonant and non-resonant amplitudes. This interference amplifies the  $N^*$  contributions to all CM-angular distributions  $d\sigma/d(-\cos(\theta_i))$  ( $i = \pi^+, \pi^-, p$ ) of the final hadrons, which improves the sensitivity of the fit to the resonance parameters. Furthermore, the shapes of the resonant and non-resonant differential cross sections are rather different, especially for the final-state angular distributions. Substantial differences in the shapes of the resonant/non-resonant contributions and their interference allow us to isolate the resonant contribution in a combined fit of all nine one-fold differential cross sections despite the relatively small resonant contributions to the fully integrated cross sections. In our previous analysis [6] we found resonant contributions to the fully integrated cross sections from 10% to 30%.

The examples of Figs. 4 and 5 demonstrate that the uncertainties of the resonance parts are comparable with those of the experimental data. This is further evidence for the credible separation between the resonant and non-resonant contributions. Any ambiguities in the evaluation of these two contributions would result in larger uncertainties for the resonant and/or non-resonant parts derived from the fit than the uncertainties of the original data. But this is not the case in the entire kinematical area covered by the CLAS  $\pi^+\pi^-p$  electroproduction measurements of Ref. [6]. Therefore, these data provide enough constraints in order to determine the resonant contributions to all differential cross sections.

##### B. $N^*$ parameters from the fit of the $\pi^+\pi^-p$ electroproduction cross sections

The procedure described in Section III allows us to extract the  $\gamma_v p N^*$  electrocouplings and their uncertainties. A special approach was developed for the evaluation of the  $P_{11}(1440)$  electrocouplings. According to the analysis [15] of the CLAS  $N\pi$  electroproduction data, the  $A_{1/2}$  electrocoupling of this resonance changes sign between  $Q^2$  of 0.40 GeV<sup>2</sup> and 0.45 GeV<sup>2</sup>. Here the  $A_{1/2}$  electrocoupling is close to zero and is an order of magnitude smaller than  $S_{1/2}$ . The  $A_{1/2}$  variations computed as a percentage of the start value, which is close to zero, become too small. For realistic uncertainty estimates we varied  $A_{1/2}$  for 0.4 GeV<sup>2</sup> <  $Q^2$  < 0.5 GeV<sup>2</sup> in the ranges shown in Table V. By varying  $A_{1/2}$  inside these widened ranges, we scanned the trial values comparable with those of  $S_{1/2}$ , as they were obtained in the analysis [15] of the CLAS  $N\pi$  electroproduction data. We refit the CLAS data of Ref. [6] on  $\pi^+\pi^-p$  electroproduction by varying  $A_{1/2}$ , as described above, keeping the variation of all



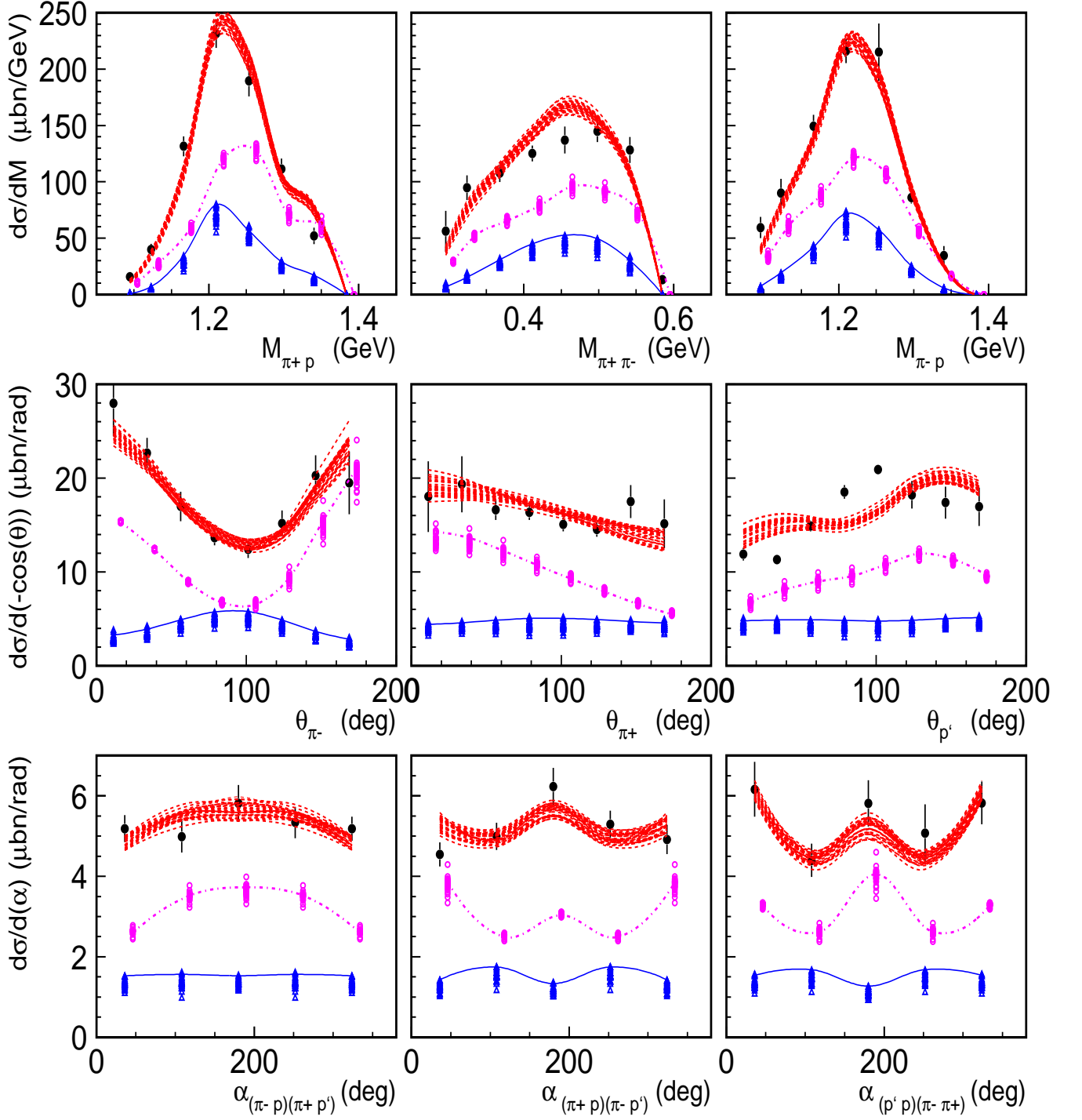


FIG. 4: (color online) Resonant (blue triangles) and non-resonant (green open circles) contributions to the differential cross sections (red lines) obtained from the CLAS data [6], fit within the framework of the JM model at  $W = 1.51$  GeV,  $Q^2 = 0.38$  GeV<sup>2</sup>. The solid blue and dotted-dashed green lines stand for the resonant and non-resonant contributions, respectively, which were computed for minimal  $\chi^2/d.p.$  achieved in the data fit. The points for resonant and non-resonant contributions are shifted on each panel for better visibility. Dashed lines show selected fits.

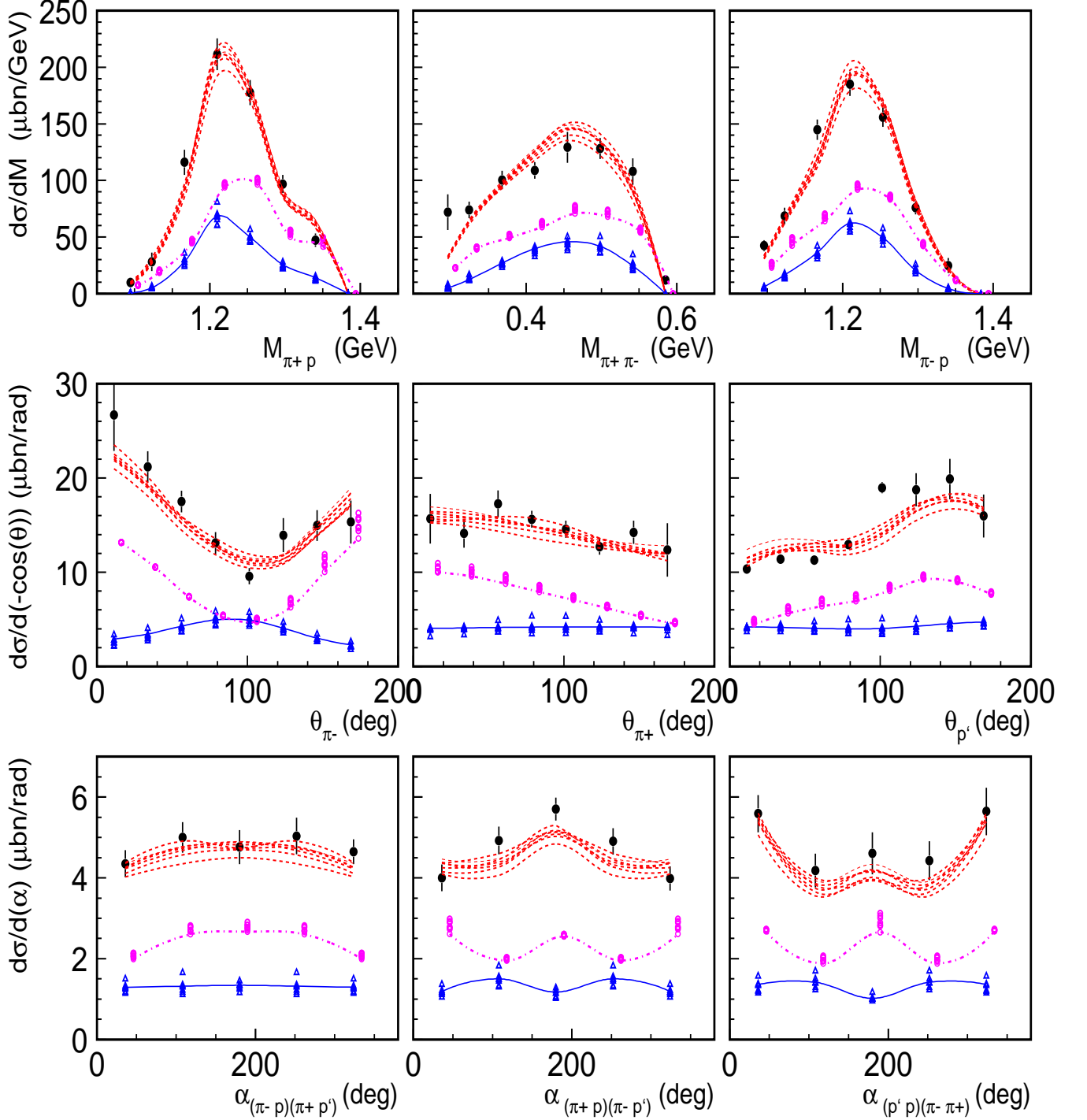


FIG. 5: (color online) The same as in Fig. 4 at  $W = 1.51$  GeV,  $Q^2 = 0.43$  GeV<sup>2</sup>.

other resonant and non-resonant parameters as described in Section III.

In order to compare our results on the  $P_{11}(1440)$  and  $D_{13}(1520)$  electrocouplings in the  $\pi^+ \pi^- p$  electroproduction channel with their values from the analysis of  $N\pi$

electroproduction [15], we have to use in both of the exclusive electroproduction channels common branching fractions for decays of these resonances to the  $N\pi$  and  $N\pi\pi$  final states. According to the RPP [53], the sum of the branching fractions into the  $N\pi$  and  $N\pi\pi$  final

$Q^2$ bins, (GeV <sup>2</sup> )	Ranges covered in variations of $A_{1/2}$ electrocoupling of the $P_{11}(1440)$ resonance, (10 <sup>-3</sup> GeV <sup>-1/2</sup> )
0.40-0.45	-20 - +5
0.45-0.50	-5 - 20

TABLE V: Variation range for the  $P_{11}(1440)$   $A_{1/2}$  electrocoupling at photon virtualities where this electrocoupling changes sign.

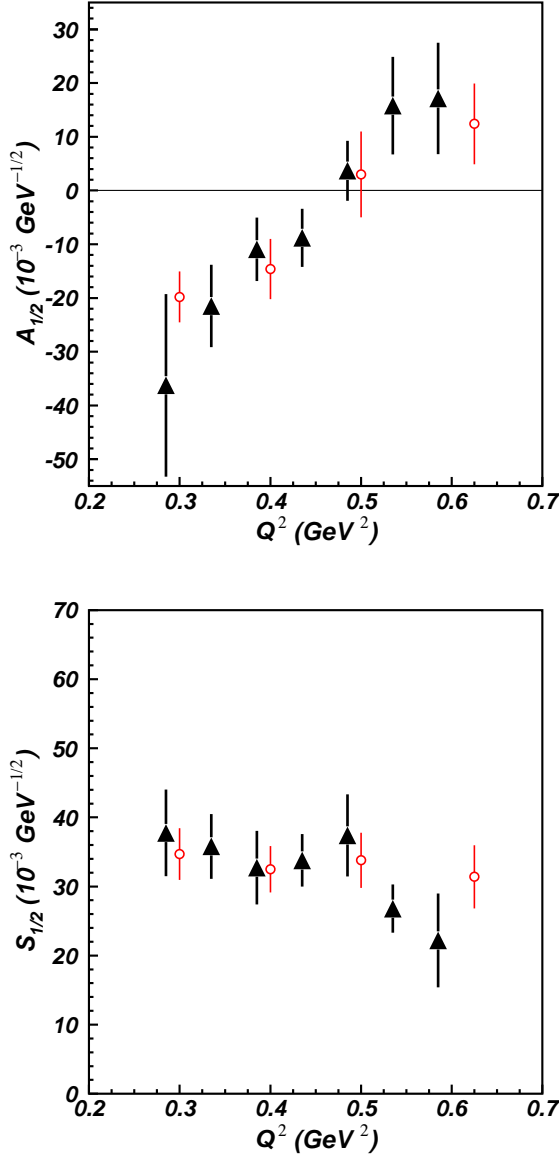


FIG. 6: (color online) Electrocouplings and full error bars of the  $P_{11}(1440)$  state. The results from the analysis of the CLAS  $\pi^+\pi^-p$  electroproduction data [6] are shown by triangles. Electrocouplings from the analysis of the  $N\pi$  electroproduction data [15] are shown by circles.

$Q^2$ , (GeV <sup>2</sup> )	$A_{1/2}$ , (10 <sup>-3</sup> GeV <sup>-1/2</sup> )	$S_{1/2}$ , (10 <sup>-3</sup> GeV <sup>-1/2</sup> )
0.28	$-36.3 \pm 17.0$	$37.8 \pm 6.3$
0.33	$-21.5 \pm 7.7$	$35.8 \pm 4.7$
0.38	$-10.9 \pm 5.9$	$32.7 \pm 5.3$
0.43	$-8.8 \pm 5.4$	$33.8 \pm 3.8$
0.48	$3.7 \pm 5.9$	$37.4 \pm 5.9$
0.53	$15.8 \pm 9.1$	$26.8 \pm 3.5$
0.58	$17.2 \pm 10.4$	$22.2 \pm 6.8$

TABLE VI: Electrocouplings of the  $P_{11}(1440)$  resonance determined from this analysis of  $\pi^+\pi^-p$  electroproduction off protons within the framework of the JM model [7].

states accounts for almost 100% of the total decay widths of the  $P_{11}(1440)$  and  $D_{13}(1520)$  states. In our analysis the branching fractions for  $P_{11}(1440)$  and  $D_{13}(1520)$  resonance decays to the  $N\pi$  final state  $BF(N\pi)$  were taken from the previous CLAS studies of  $N\pi$  electroproduction data [15], since the  $N\pi$  exclusive electroproduction channels are most sensitive to contributions from the  $P_{11}(1440)$  and  $D_{13}(1520)$  resonances. The unitarity condition allows us to estimate the branching fraction  $BF(N\pi\pi)_{corr}$  value as:

$$BF(N\pi\pi)_{corr} = 1 - BF(N\pi). \quad (14)$$

For these resonance decays to the  $N\pi\pi$  final states it turns out that the estimated branching fractions  $BF(N\pi\pi)_{corr}$  from Eq. (14) are slightly ( $< 10\%$ ) different with respect to those obtained from the  $\pi^+\pi^-p$  fit ( $BF(N\pi\pi)_0$ ). Therefore, we multiplied the  $\pi\Delta$  and  $\rho p$  hadronic decay widths of  $P_{11}(1440)$  and  $D_{13}(1520)$  from the  $\pi^+\pi^-p$  fit by the ratio  $\frac{BF(N\pi\pi)_{corr}}{BF(N\pi\pi)_0}$  in order to make them consistent with the unitarity condition of Eq. (14).

Consequently, the  $P_{11}(1440)$  and  $D_{13}(1520)$  electrocouplings obtained in our analysis are multiplied by correction factors

$$C_{hd} = \sqrt{\frac{BF(N\pi\pi)_0}{BF(N\pi\pi)_{corr}}}, \quad (15)$$

in order to keep the resonant parts and the full computed differential  $\pi^+\pi^-p$  cross sections unchanged under the re-scaling of resonance hadronic decay parameters described above.

The  $P_{11}(1440)$  and  $D_{13}(1520)$  electrocouplings derived from the fit of  $\pi^+\pi^-p$  electroproduction data are presented in Tables VI and VII. The masses and hadronic decay parameters are shown in Tables VIII and IX. The hadronic resonance parameters are taken as the average of their values obtained in independent fits in the three  $Q^2$  intervals shown in Table IV.

In Figures 6 and 7 we compare the results of this analysis with results of the analysis of CLAS  $N\pi$  electroproduction data [15]. Furthermore, there are also the  $P_{11}(1440)$  and  $D_{13}(1520)$  electrocouplings available from the MAID partial wave analysis of  $N\pi$  electroproduction

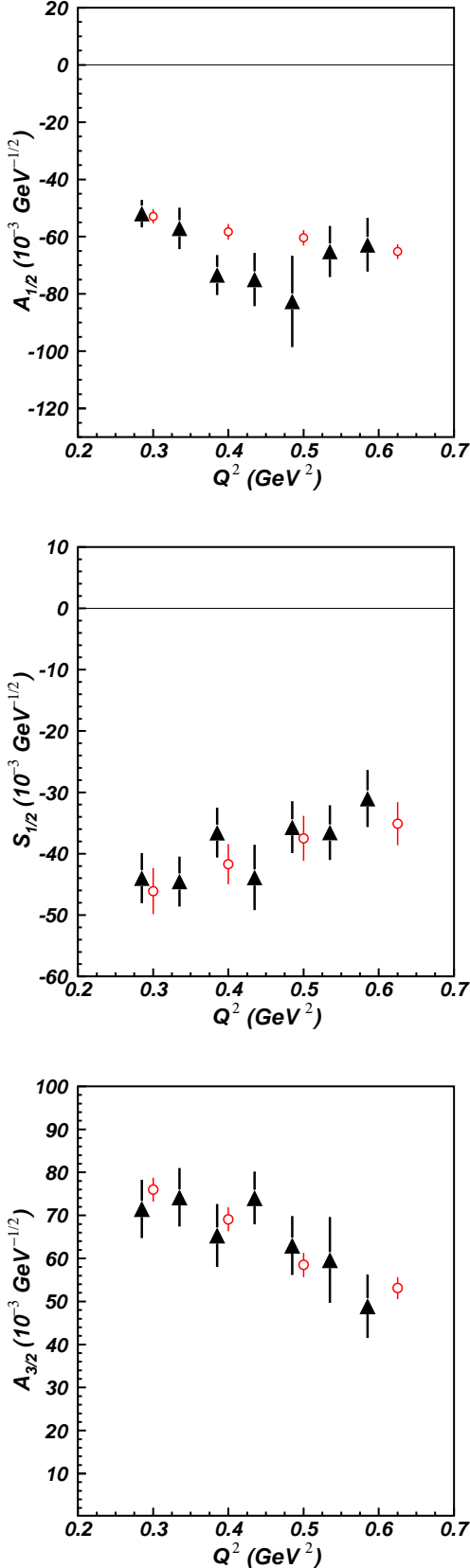


FIG. 7: (color online) Electrocouplings and full error bars of the  $D_{13}(1520)$  state. This analysis of the CLAS  $\pi^+\pi^-p$  electroproduction data [6] is shown by triangles. Electrocouplings from the analysis of the  $N\pi$  electroproduction data [15] are shown by circles.

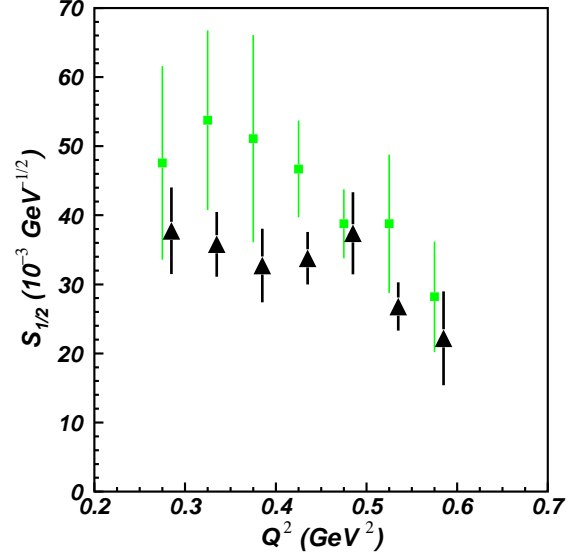


FIG. 8: (color online) Comparison between the final results on  $S_{1/2}$  electrocouplings for the  $P_{11}(1440)$  from this analysis of CLAS  $\pi^+\pi^-p$  electroproduction data [6] (triangles) with the values obtained by employing a regular BW ansatz for the resonant amplitudes and with the contributions from the  $S_{11}(1535)$  state turned off (squares).

$Q^2$ , ( $\text{GeV}^2$ )	$A_{1/2}$ , ( $10^{-3} \text{ GeV}^{-1/2}$ )	$S_{1/2}$ , ( $10^{-3} \text{ GeV}^{-1/2}$ )	$A_{3/2}$ , ( $10^{-3} \text{ GeV}^{-1/2}$ )
0.28	$-51.9 \pm 4.8$	$-44.0 \pm 4.1$	$71.5 \pm 6.8$
0.33	$-57.1 \pm 7.2$	$-44.5 \pm 4.1$	$74.2 \pm 6.8$
0.38	$-73.4 \pm 7.0$	$-36.5 \pm 4.1$	$65.3 \pm 7.3$
0.43	$-75.0 \pm 9.3$	$-43.9 \pm 5.3$	$74.1 \pm 6.1$
0.48	$-82.6 \pm 15.9$	$-35.7 \pm 4.2$	$63.0 \pm 6.8$
0.53	$-65.2 \pm 8.9$	$-36.6 \pm 4.5$	$59.6 \pm 10.0$
0.58	$-62.2 \pm 9.3$	$-31.0 \pm 4.6$	$48.9 \pm 7.4$

TABLE VII: Electrocouplings of the  $D_{13}(1520)$  resonance determined from this analysis of  $\pi^+\pi^-p$  electroproduction off protons within the framework of the JM model [7].

at  $Q^2 < 0.6 \text{ GeV}^2$  [60–62]. Our analysis confirms the sign change of the  $A_{1/2}$  electrocoupling for the  $P_{11}(1440)$ , first observed in the  $N\pi$  channels. We found the zero-crossing to be between  $Q^2=0.4 \text{ GeV}^2$  and  $0.45 \text{ GeV}^2$  in agreement with the  $N\pi$  analysis [15]. The electrocouplings for the  $P_{11}(1440)$  and  $D_{13}(1520)$  are also consistent within their uncertainties with the CLAS analysis of the  $N\pi$  electroproduction [15] with the exception of the  $A_{1/2}$  amplitude of  $D_{13}(1520)$ , where we see a difference in the range of  $0.4 \text{ GeV}^2 < Q^2 < 0.5 \text{ GeV}^2$ , which is slightly larger than a standard deviation. In this range of  $Q^2$  two different analyses of the  $N\pi$  exclusive channels the CLAS [15] and the MAID [60], give also slightly different values of the  $A_{1/2}$  electrocoupling for the  $D_{13}(1520)$ . The MAID results are close to our extraction at  $0.4 \text{ GeV}^2 < Q^2 <$



Parameter	Analysis of the CLAS $\pi^+\pi^-p$ data	RPP
Breit-Wigner mass, MeV	$1458 \pm 12$	1420-1470 ( $\approx 1440$ )
Breit-Wigner width, MeV	$363 \pm 39$	200-450 ( $\approx 300$ )
$\pi\Delta$ partial decay width, MeV	$142 \pm 48$	
$\pi\Delta$ BF,	23%-58%	20%-30%
$\rho p$ partial decay width, MeV	$6.2 \pm 4.1$	
$\rho p$ BF	$< 2.0\%$	$< 8.0\%$

TABLE VIII: Hadronic parameters of the  $P_{11}(1440)$  resonance determined from the CLAS data [6] on  $\pi^+\pi^-p$  electroproduction off protons within the framework of the JM model [7] and from the RPP [53].

Parameter	Analysis of the CLAS $\pi^+\pi^-p$ data	RPP
Breit-Wigner mass, MeV	$1521 \pm 4$	1515-1525 ( $\approx 1520$ )
Breit-Wigner width, MeV	$127 \pm 4$	100-125 ( $\approx 115$ )
$\pi\Delta$ partial decay width, MeV	$35 \pm 4$	
$\pi\Delta$ BF	24%-32%	15%-25%
$\rho p$ partial decay width, MeV	$16 \pm 5$	
$\rho p$ BF	8.4%-17%	15%-25%

TABLE IX: Hadronic parameters of the  $D_{13}(1520)$  resonance determined from the CLAS data [6] on  $\pi^+\pi^-p$  electroproduction off protons within the framework of the JM model [7] and from the RPP [53].

0.5 GeV<sup>2</sup>, but start to deviate at larger photon virtualities. Instead, for the other electrocouplings of  $D_{13}(1520)$ , both the CLAS [15] and the MAID [60] analyses of the  $N\pi$  channels are consistent with the results of this analysis.

The unitarization of the resonant amplitudes and the contribution from the  $S_{11}(1535)$  state have a negligible impact on  $A_{1/2}$  for  $P_{11}(1440)$  and on all  $D_{13}(1520)$  electrocouplings. However, both factors affect the  $S_{1/2}$  electrocouplings of  $P_{11}(1440)$ . Figure 8 shows a comparison of the  $P_{11}(1440)$   $S_{1/2}$  electrocouplings obtained with the unitarized BW ansatz incorporating the  $S_{11}(1535)$  contributions versus the regular BW ansatz without the  $S_{11}(1535)$ . The implementation of the  $S_{11}(1535)$  contributions imposes additional constraints on the ranges of the  $P_{11}(1440)$   $S_{1/2}$  electrocouplings that correspond to the computed differential cross sections, which are consistent with the data, allowing us to improve the uncertainties in the extraction of this electrocoupling.

Consistent results on the electrocouplings of the  $P_{11}(1440)$  and  $D_{13}(1520)$  resonances, which are available for the first time from independent analyses of the major  $N\pi$  and  $\pi^+\pi^-p$  exclusive channels provide evidence for the reliable extraction of these fundamental quantities from the experimental data. Furthermore, this agreement strongly supports the reaction models employed for the analyses of the  $N\pi$  [15] and  $\pi^+\pi^-p$  [7] electroproduction data.

The Breit-Wigner masses and mean values for the total decay widths of the  $P_{11}(1440)$  and  $D_{13}(1520)$ , derived from the  $\pi^+\pi^-p$  data and listed in Tables VIII and IX, are in a good agreement with those reported in the RPP [53]. Uncertainties in the total resonance decay widths

were obtained by varying the  $\pi\Delta$  and  $\rho p$  partial decay widths, while the decay width to the  $N\pi$  final state remained fixed at the values taken from Ref. [15]. In comparison with the results in the RPP [53], our analysis gives somewhat larger branching fractions to the  $\pi\Delta$  final states for the hadronic decays of both the  $P_{11}(1440)$  and  $D_{13}(1520)$  states, and a smaller hadronic decay to the  $\rho p$  final state.

Both  $\gamma_v p N^*$  electrocouplings and resonance hadronic decay widths are obtained at the resonant point on the real energy axis  $W = M_r$ , using the relativistic Breit-Wigner parametrizations of the resonant amplitudes. All resonance parameters determined in our approach incorporate *all* relevant contributions to the  $N^*$  structure. The extraction from the data of the individual contributions of the quark core and the meson-baryon dressing is outside of our scope. Our results can be compared directly with those determined from other meson electroproduction channels, where the BW ansatz for resonant amplitudes is used. For comparisons with results obtained from models that use other ways to describe the resonant contributions, the resonant cross sections at the resonant points can be compared.

## V. THE IMPACT ON THE STUDIES OF RESONANCE STRUCTURE FROM THE CLAS RESULTS ON THE $P_{11}(1440)$ AND $D_{13}(1520)$ ELECTROCOUPLINGS AND HADRONIC PARAMETERS.

In this section we discuss the impact of the CLAS data on the  $P_{11}(1440)$  and  $D_{13}(1520)$  electrocouplings and hadronic parameters determined from the indepen-

dent analyses of  $N\pi$  and  $\pi^+\pi^-p$  electroproduction off protons on the contemporary understanding of the structures these states at various distances.

### A. $P_{11}(1440)$ resonance

The first comprehensive  $P_{11}(1440)$  electrocoupling sets available from the CLAS data on  $N\pi$  and  $\pi^+\pi^-p$  electroproduction provide access to the active degrees of freedom in the  $P_{11}(1440)$  structure at various distances. Previous studies [13, 15] already showed a strong sensitivity of the electrocouplings to assumptions about the active components contributing to the  $P_{11}(1440)$  structure.

The  $P_{11}(1440)$  resonance is characterized by peculiar features:

- a smaller mass (1440 MeV) than that expected by quark models with vector flavor-conserving quark-quark ( $qq$ ) interactions, this is less than the mass of the first orbital excitation of the nucleon, the  $S_{11}(1535)$ , leading to so-called wrong  $P_{11}(1440)/S_{11}(1535)$  mass ordering [1], and
- a large hadronic decay width of  $\approx 300$  MeV, although other resonances with masses below 1.6 GeV have decay widths of less than 200 MeV,

that make it difficult to describe the  $P_{11}(1440)$  as a pure three quark bound state. To the best of our knowledge, there are no models, incorporating only quark degrees of freedom, capable of describing simultaneously the mass ordering of the  $P_{11}(1440)$  and  $S_{11}(1535)$  resonances, the unusually large  $P_{11}(1440)$  hadronic decay width, and the photo and electrocouplings. Therefore, different approaches for the description of the  $P_{11}(1440)$  were developed that take into account the contributions from degrees of freedom other than those of dressed quarks [17, 23, 63, 76]. The CLAS results on the  $P_{11}(1440)$  electrocouplings of [15] and this analysis allows for the first time to confront the model expectations for the  $P_{11}(1440)$  structure with the experimental data, in particular at  $Q^2 < 0.6$  GeV<sup>2</sup>, where consistent results from the independent analyses of  $N\pi$  and  $\pi^+\pi^-p$  electroproduction off protons have now become available.

In Ref. [63] the  $Q^2$ -dependence of the  $P_{11}(1440)$  electrocouplings was obtained by assuming a hybrid nature of this resonance. In this approach, the  $P_{11}(1440)$  is treated as a resonance dominated by a single SU(6) configuration of three dressed quarks oscillating against an explicitly excited glue, denoted  $q^3G$ . The  $P_{11}(1440)$  as a hybrid state has a spin-flavor part of the wave function orthogonal to that of the nucleon, whereas the spin-flavor part of wave function for the  $P_{11}(1440)$ , as a radially excited three quark state, is identical to that of the nucleon. This difference makes it possible to distinguish between the  $P_{11}(1440)$  as a regular  $q^3$  or hybrid  $q^3G$  state by studying the  $Q^2$ -evolution of the  $P_{11}(1440)$  electrocouplings. A characteristic prediction of [63] for the hybrid origin of

the  $P_{11}(1440)$  is the absence of the longitudinal coupling, i.e.  $S_{1/2} = 0$ . This is a consequence of negligible SU(6) configuration mixing in the non-relativistic approximation adopted in [63] for the description of the  $P_{11}(1440)$  structure. The recent Lattice QCD (LQCD) studies of the  $N^*$  spectrum [33, 34] also confirmed the presence of the leading SU(6)-spin-flavor-configuration in the structure of  $P_{11}(1440)$ . The  $S_{1/2} = 0$  values for  $P_{11}(1440)$  are clearly in disagreement with the results of our analysis of the  $\pi^+\pi^-p$  electroproduction data (see Fig. 6), showing that at small photon virtualities  $S_{1/2}$  is larger than  $A_{1/2}$ , or at least comparable at  $Q^2$  close to zero. This allows us to rule out sizable hybrid contributions to the  $P_{11}(1440)$ , confirming the conclusions from our previous analysis of the  $N\pi$  final state [15]. The lack of a substantial contribution of a hybrid component to the lowest mass resonances in the  $P_{11}$  partial wave was also confirmed in the LQCD studies [34].

The previous analysis [15] of the  $N\pi$  CLAS data showed that the most satisfactory description of the  $P_{11}(1440)$  electrocouplings was achieved at  $Q^2 > 1.5$  GeV<sup>2</sup> within the framework of relativistic light-front quark models [10, 13], as shown in Fig. 9. In these models, the  $P_{11}(1440)$  electrocouplings are evaluated from the fully covariant, one-body electromagnetic transition current for point-like constituent quarks in the impulse approximation, employing light-front relativistic Hamiltonian dynamics [64–66]. Resonance electrocouplings are computed in a frame where the “+” component of the virtual photon light-cone momenta is equal to zero. For this particular choice, the contribution from  $q\bar{q}$  pairs into photon propagation are eliminated [13]. In these models [10, 13] the  $P_{11}(1440)$  is treated as the first radial excitation of three constituent quarks. The wave function of the ground state and  $P_{11}(1440)$  are described under the simplifying assumption, that they are unmixed single oscillator basis states.

A reasonable description of the CLAS data at  $Q^2 > 1.5$  GeV<sup>2</sup> is achieved in both models [10, 13], as seen in Fig. 9. Accounting for the relativistic transition operator is important in order to describe the CLAS data over the entire range of photon virtualities, and especially at small  $Q^2$  where the sign of  $A_{1/2}$  changes [10, 13], although a quantitative description of the data at small  $Q^2$  has not been achieved (see Fig. 9).

A similarly good description of the  $P_{11}(1440)$  electrocouplings at  $Q^2 > 1.5$  GeV<sup>2</sup> was found using a valence quark model [67] based on the covariant spectator formalism [68, 69]. The results of this model are also shown in Fig. 9. Incorporating three constituent quarks only, this model treats the  $N^*$  electroexcitation as a virtual photon interaction with a valence quark in the ground state, while the two other quarks are combined to a spectator diquark in both spin states 0 and 1. The wave function of the ground state is parametrized and fit to the data on elastic nucleon form factors. The  $P_{11}(1440)$  structure is described as the first radial excitation of the nucleon ground state quarks. With no additional parameters,

the wave function of the  $P_{11}(1440)$  was calculated employing the orthogonality condition between the ground state and the  $P_{11}(1440)$  wave functions. The electrocouplings of  $P_{11}(1440)$  are calculated for the valence quark transition between the nucleon ground state and its first radial excitation. As shown in Fig. 9, this model [67] describes the trend of the CLAS data for  $Q^2 > 1.5 \text{ GeV}^2$ .

Different approaches to describe the  $P_{11}(1440)$  resonance using structureless constituent quarks of non-running masses – two relativistic light front quark models [10, 13] and a valence quark model [67] – are capable of reproducing the major features of the CLAS data on  $P_{11}(1440)$  electrocouplings only for  $Q^2 > 1.5 \text{ GeV}^2$ . These approaches fail to describe the electrocouplings for  $Q^2 < 1.0 \text{ GeV}^2$ . On the other hand, consistent results on  $P_{11}(1440)$  electrocouplings from the independent analyses of  $N\pi$  and  $\pi^+\pi^-p$  electroproduction off protons at  $Q^2 < 0.6 \text{ GeV}^2$  emphasize the credibility of the experimental data and the inability of describing the  $P_{11}(1440)$  structure by only accounting for quark degrees of freedom without meson-baryon dressing.

The global analysis of  $N\pi$ , photo-, electro-, and hadroproduction within the framework of the EBAC-DCC coupled-channel approach [17, 18, 23, 70–73] revealed this additional component in the  $N^*$  structure that is most relevant at  $Q^2 < 1.0 \text{ GeV}^2$ . The general unitarity condition for full meson electroproduction amplitudes requires contributions from non-resonant meson electroproduction and hadronic scattering amplitudes to the  $\gamma_v p N^*$  vertex, as depicted in Fig. 10. This contribution incorporates all possible intermediate meson-baryon states and subsequent meson-baryon scattering processes that eventually result in the  $N^*$  formation. As was mentioned in Section IV, the  $\gamma_v p N^*$  electrocouplings extracted in our analysis of  $\pi^+\pi^-p$  electroproduction data, as well as in the previous analysis of the  $N\pi$  data [15] account for *all* contributions to the resonance structure, including for those from meson-baryon dressing. Instead, most of quark models, including aforementioned [10, 13, 67], account only for the quark-core component in  $N^*$  photo-/electroexcitation, while meson-baryon dressing, being a part of the reaction mechanism, is completely outside of their scope. Therefore, the current and the previous CLAS results [15] on  $\gamma_v p N^*$  electrocouplings should be different with respect to those from the quark model expectations in  $Q^2$ -areas where the contributions from meson-baryon dressing are substantial.

In Ref. [17] the meson-baryon dressing amplitudes are calculated from diagrams describing non-resonant mechanisms in  $N\pi$  photo-, electro-, and hadroproduction channels with hadronic parameters fit to the world meson hadroproduction data. The estimates of the absolute values for meson-baryon dressing contributions to the  $P_{11}(1440)$  electrocouplings showed that meson-baryon dressing amplitudes are maximal at  $Q^2 < 1.0 \text{ GeV}^2$ .

Therefore the meson-baryon dressing contributions could be responsible for the differences observed in this

area between the CLAS data on the  $N^*$  electrocouplings and the quark model expectations of Refs. [10, 13, 67]. The meson-baryon dressing decreases with  $Q^2$  and in the region  $Q^2 > 1.0 \text{ GeV}^2$  we have a gradual transition to the dominance of quark degrees of freedom, as indicated by the better description of the  $P_{11}(1440)$  electrocouplings within the framework of quark models.

Evaluations for bare-quark-core contributions to the dressed  $P_{11}(1440)$  electrocouplings have recently been obtained within the framework of QCD-based Dyson-Schwinger Equations (DSEQCD) [41]. The DSEQCD results are close to the bare-quark-core contributions to the  $P_{11}(1440)$  electrocouplings extracted from the experimental data within the framework of the EBAC-DCC coupled-channel approach [23] and far from the dressed  $P_{11}(1440)$  electrocouplings obtained in our analysis. This DSEQCD result offers further evidence for substantial contributions from meson-baryon dressing to the  $P_{11}(1440)$  electrocouplings.

We conclude that the structure of  $P_{11}(1440)$  is determined by the combined contributions from an internal quark core of constituent quarks in the first radial excitation and an external meson-baryon dressing, the latter being most relevant at small  $Q^2$ .

Lattice QCD is making progress in calculating  $\gamma_v N N^*$  transition form factors from first QCD principles. Exploratory calculations of the  $\gamma_v p P_{11}(1440)$  transition form factors  $F_{1,2}^{P_{11}}(Q^2)$  were carried out within LQCD in the quenched approximation using a pion mass of 500 MeV and a simplified set of projection operators [29, 30]. Despite the aforementioned simplifications, the first LQCD evaluations are in approximate agreement with the CLAS  $F_{1,2}^{P_{11}}(Q^2)$  form factor results at  $Q^2 > 1.5 \text{ GeV}^2$ . Improved LQCD calculations with dynamical quarks and a smaller pion mass of 380 MeV [31, 32] provide for the first time a reasonable description of the CLAS data for  $Q^2 < 1.0 \text{ GeV}^2$ . These studies demonstrated promising opportunities to relate the results on the  $Q^2$ -evolution of the  $\gamma_v p N^*$  electrocouplings directly to QCD.

Together with the recent LQCD [33, 34] and DSEQCD [38] results on the  $N^*$  spectrum and the first DSEQCD results on bare  $\gamma_v p P_{11}(1440)$  electrocouplings [41], this is an important step toward to our understanding of baryon formation and the nature of confinement from the first principles of QCD.

The  $\pi\Delta$  and  $\rho p$   $P_{11}(1440)$  hadronic decay widths obtained in our analysis are listed in Table VIII and compared with RPP [53] values. The quark models, which describe  $N^*$  hadronic decays through flux tube breaking [74, 75], provide a good description of our  $\pi\Delta$  and  $\rho p$  decay widths of 100 and 2.5 MeV, respectively. However, the flux-tube breaking mechanism is unable to describe the  $P_{11}(1440)$   $N\pi$  hadronic decays. It predicts a width of approximately 400 MeV for this channel, which is in strong disagreement with measured values [53]. Other approaches, listed in Ref. [16], fail to describe the  $N\pi\pi$  hadronic decay widths.

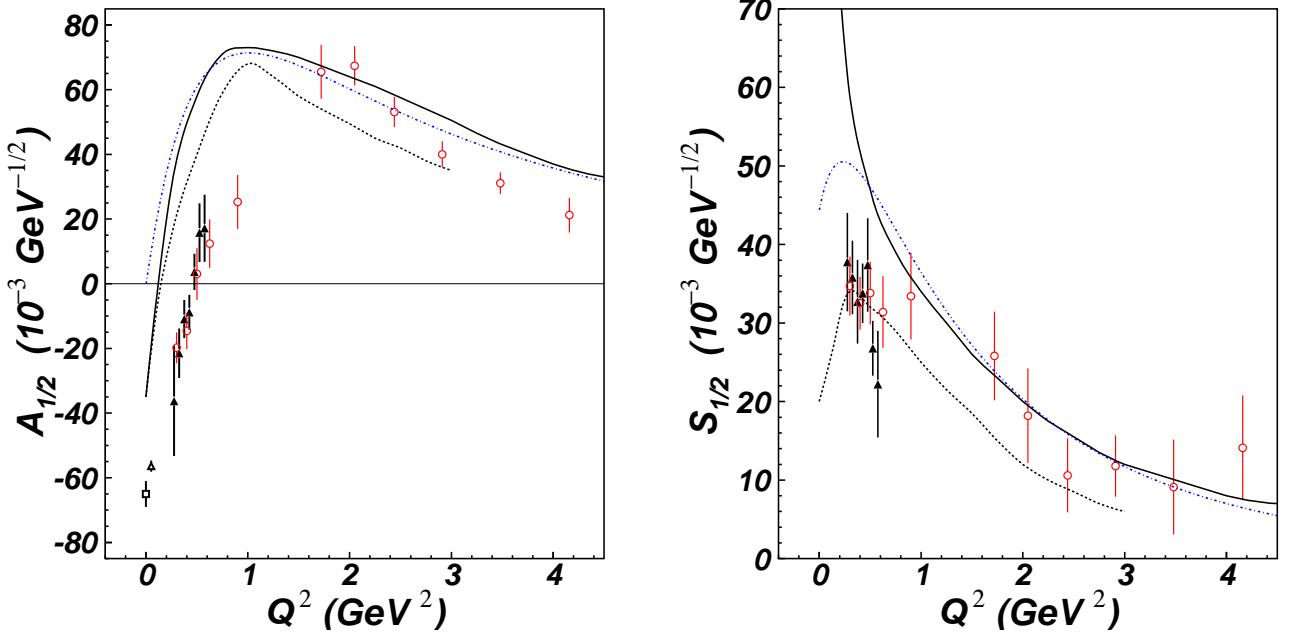


FIG. 9: (color online) Photo- and electrocouplings of the  $P_{11}(1440)$  resonance in comparison with predictions of quark models. The photocouplings are taken from RPP [53] (open square) and the CLAS data analysis [59] (open triangle). Other data points are the same as in Fig. 6. The results of relativistic light-front quark models [10, 13] are shown by solid and dashed lines, respectively. Results of the covariant valence quark spectator diquark model [67] are shown by the dashed dotted line.

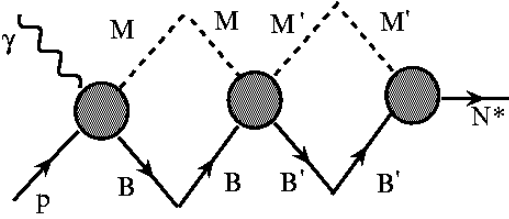


FIG. 10: Processes that contribute to meson-baryon dressing in the  $N^*$  photo/electroexcitations within the EBAC-DCC approach.

To date the quantitative description of  $P_{11}(1440)$  hadronic decays remains a challenging problem. Consistent accounting for the meson-baryon dressing contributions to both electromagnetic and hadronic  $P_{11}(1440)$  vertices is important to gain insight into the structure of this excited state [20, 21, 41, 76].

### B. $D_{13}(1520)$ resonance

Analyses of the previous CLAS data [15] on  $D_{13}(1520)$  electrocouplings determined from  $N\pi$  exclusive electroproduction channels, showed that their satisfactory description for  $Q^2 > 1.5 \text{ GeV}^2$  can be achieved within the

framework of the hypercentral constituent quark model (hCQM) [77] (solid lines in Fig. 11). In this model the central confinement potential is parametrized by a sum of Coulomb and linear terms expressed in collective hypercoordinates for the three constituent quark system. The use of hypercoordinates effectively accounts for three-body effects in quark interactions. The remaining interaction between pairs of quarks is parametrized by a superposition of spin- and isospin-dependent hyperfine terms. Wave functions for resonances are obtained by diagonalizing the Hamiltonian in a non-relativistic approximation. Three parameters of the hCQM were fit to data on the baryon spectrum. With these parameters electrocouplings of all well-established excited nucleon states were evaluated for  $Q^2 < 5.0 \text{ GeV}^2$ , employing non-relativistic electromagnetic transition operators. The results obtained for the  $D_{13}(1520)$  state are shown in Fig. 11.

The hCQM model can describe the data trends for the  $D_{13}(1520)$  electrocouplings for  $Q^2 > 1.5 \text{ GeV}^2$ . Pronounced differences between hCQM expectations and the  $D_{13}(1520)$  electrocouplings at smaller  $Q^2$  offer an indication for contributions from active degrees of freedom other than a core of three dressed quarks to this state's electrocouplings. Meson-baryon dressing amplitudes are likely contributors in this area of photon virtualities. According to the EBAC analysis [17], for the  $D_{13}(1520)$  state they are maximal for small photon virtualities and decrease with  $Q^2$ . The EBAC analysis also



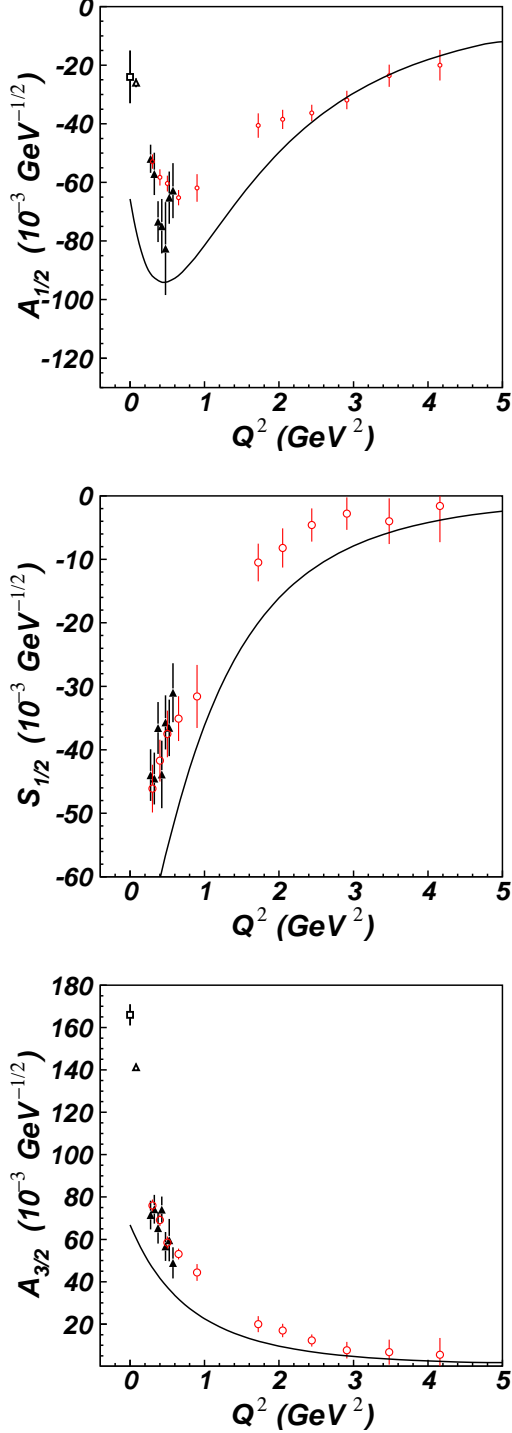


FIG. 11: (color online) Description of the CLAS data on  $D_{13}(1520)$  electrocouplings within the hQCM (solid lines) [77]. The symbols associated with the experimental data are the same as in Fig. 9.

suggests negligible meson-baryon dressing or dominant quark core contributions to the  $A_{1/2}$  electrocoupling of the  $D_{13}(1520)$  state for  $Q^2 > 1.5 \text{ GeV}^2$ , where we already have the CLAS results on this electrocoupling [15]. These results thus offer access to quark degrees of freedom in the structure of  $D_{13}(1520)$  and open up new prospects to study the dynamical dressed quark mass, structure, and their strong interactions, that are responsible for the  $N^*$  formation. These studies are of particular importance to understand the nature of confinement in the baryon sector based on QCD [28, 29, 31, 35, 38–40, 78].

Our analysis confirms a rapid helicity switch from the dominance of the  $A_{3/2}$  electrocoupling at the photon point to a comparable contribution from both transverse electrocouplings at  $Q^2 \approx 0.5 \text{ GeV}^2$  as already observed in [15]. This is shown in Fig. 12 in terms of the helicity asymmetry, defined as

$$A_{hel} = \frac{A_{1/2}^2 - A_{3/2}^2}{A_{1/2}^2 + A_{3/2}^2}. \quad (16)$$

This particular feature is expected for the contributions from the core of three constituent quarks in the first orbital nucleon excitation  $L = 1$  [79]. It suggests a significant contribution from the core of three constituent quarks to the transverse  $D_{13}(1520)$  electrocouplings even at small  $Q^2$ .

We conclude that the  $Q^2$ -evolution of the  $D_{13}(1520)$  electrocouplings is consistent with contributions of both an external meson-baryon cloud and an internal core of three constituent quarks.

The  $N\pi\pi$  hadronic decay widths of  $D_{13}(1520)$ , obtained from the CLAS  $\pi^+\pi^-p$  data, are given in the Table IX. They are close to the RPP [53] values. However, the branching fraction to the  $\pi\Delta$  final state is larger and to the  $\rho p$  final state is smaller than the RPP average. Our results on the  $N\pi\pi$  hadronic couplings of the  $D_{13}(1520)$  are well described by the flux tube breaking model of [74, 75], as well as within the framework of the  $^3P_0$  pair creation model of [80]. The success of these models indicates a substantial role of the quark core in hadronic decays of the  $D_{13}(1520)$  state.

## VI. SUMMARY AND OUTLOOK

The analysis of a large body of differential and fully integrated cross sections for the process  $\gamma^* p \rightarrow \pi^+\pi^-p$  carried out within the framework of the JM model in our previous paper [7] allowed us to establish all essential mechanisms that contribute to this exclusive channel for  $1.3 \text{ GeV} < W < 1.6 \text{ GeV}$  and  $0.2 \text{ GeV}^2 < Q^2 < 0.6 \text{ GeV}^2$ . In this paper we use the reaction model of Ref. [7] in order to determine the resonant and non-resonant contributions to the  $\pi^+\pi^-p$  differential cross sections measured with the CLAS detector [6] and eventually to obtain the  $A_{1/2}$ ,  $S_{1/2}$ , and  $A_{3/2}$  electrocouplings, as well as the  $\pi\Delta$  and  $\rho p$  decay widths for the  $P_{11}(1440)$  and  $D_{13}(1520)$  excited proton states from this data fit.

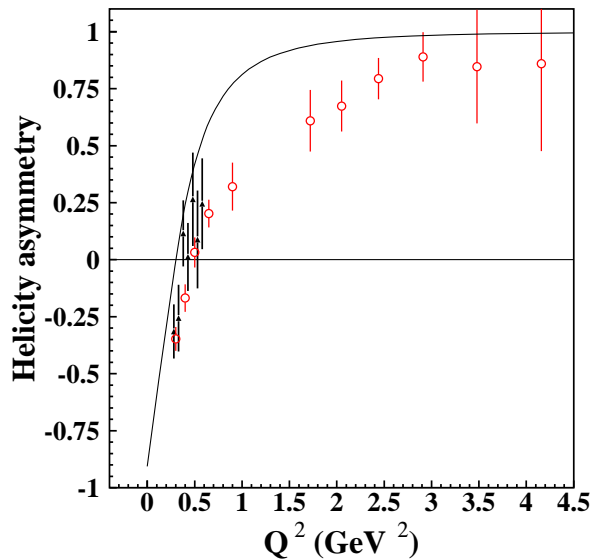


FIG. 12: (color online) Helicity asymmetry  $A_{hel}$  of Eq. (16) for the transverse electrocouplings of the  $D_{13}(1520)$  from this analysis of  $\pi^+\pi^-p$  (filled triangles) and  $N\pi$  (open circles) exclusive electroproduction channels measured with CLAS. The curve represents the non-relativistic quark model calculations [79].

The good description of all measured observables makes it possible to evaluate the resonant contributions to the cross sections, which are needed to extract the  $\gamma_v p N^*$  electrocouplings. Resonance electrocouplings and hadronic decay parameters were determined using a unitarized BW ansatz for the resonant amplitudes, that takes into account interactions between the same and different excited states in the dressed resonance propagators.

For the first time electrocouplings of the  $P_{11}(1440)$  and  $D_{13}(1520)$  resonances were obtained from the analysis of the  $\pi^+\pi^-p$  exclusive electroproduction at photon virtualities  $0.25 \text{ GeV}^2 < Q^2 < 0.60 \text{ GeV}^2$ . They are in reasonable agreement with the electrocoupling values obtained in the previous CLAS analysis of the exclusive  $N\pi$  electroproduction channels [15]. Single and charged double pion electroproduction channels represent two major contributors to meson electroproduction in the kinematical region covered by our measurements. The non-resonant mechanisms in these exclusive channels are completely different. A successful description of a large body of observables in single and charged double pion electroproduction channels with consistent values of the  $P_{11}(1440)$  and  $D_{13}(1520)$  electrocouplings confirms that the  $\gamma_v p N^*$  electrocouplings can be reliably determined in independent analyses of these electroproduction channels. A good agreement between electrocouplings of the aforementioned excited states obtained from  $N\pi$  and  $\pi^+\pi^-p$  electroproduction also demonstrate that the reac-

tion models developed to describe these exclusive channels [7, 15] can be used to determine electrocouplings of most of the excited proton states that decay preferentially into either  $N\pi$  or  $N\pi\pi$  final states.

The  $\pi\Delta$  and  $\rho p$  partial hadronic decay widths of the  $P_{11}(1440)$  and  $D_{13}(1520)$  states were also determined. They are close to the results of experiments with hadronic probes reported in the RPP [53].

The comparison of the CLAS data on  $P_{11}(1440)$  and  $D_{13}(1520)$  electrocouplings with the expectations of conceptually different quark models [10, 13] and [67], complemented by evaluations of meson-baryon dressing [17] allowed us to shed light on the relevant components in the structure of these states and to explore their evolution with photon virtualities. The electrocouplings reveal two major contributions, from an internal core of three dressed quarks and an external meson-baryon cloud.

The structure of the  $P_{11}(1440)$  is consistent with a combined contribution from constituent quarks in the first radial excitation and from a meson-baryon cloud with pronounced contributions at  $Q^2 < 0.6 \text{ GeV}^2$ . The electrocouplings of the  $D_{13}(1520)$  contain a combined contribution of three constituent quarks in the first orbital nucleon excitation  $L = 1$  and an external meson-baryon cloud, which becomes negligible for the  $A_{1/2}$  electrocoupling of  $D_{13}(1520)$  for  $Q^2 > 1.5 \text{ GeV}^2$ . The CLAS results on the  $A_{1/2}$  electrocoupling of the  $D_{13}(1520)$  resonance in this kinematical region provide direct access to quark degrees of freedom in the structure of this excited state. A physical interpretation of these results is of particular interest for those who are studying hadron structure starting from the QCD Lagrangian [28, 29, 31–35, 41, 78].

The resonance electrocouplings and hadronic decay parameters presented in this paper were obtained using the unitarized BW parametrization of resonant amplitudes. Their values are determined at the resonant point on the real energy axis ( $W = M_r$ ) and incorporate *all* combined relevant contributions (quark-core, meson-baryon dressing and so on). The  $N^*$  parameters extracted from the data in this way can only be compared directly with those obtained from the same or other exclusive channel data fits that employ BW parametrizations of resonant amplitudes. It remains to be seen how these resonance parameters can be related to the values determined from singularities of the reaction amplitudes in the complex energy plane, as employed in coupled-channel analyses [23]. In the Section II C we described the JM model relations between the resonance parameters and the model independent observables: the resonant part of the cross sections and  $N^*$  electromagnetic/hadronic decay widths. We can use the model independence of these observables and require agreement of the cross section and/or resonance decay widths at the resonant point evaluated in different models. These observables, in turn, could be related to the resonance parameters for any particular model. This should make it possible to establish relations between resonant parameters determined in our approach

and those from a global multi-channel analyses.

## VII. ACKNOWLEDGMENTS

We would like to acknowledge the outstanding efforts of the staff of the Accelerator and the Physics Divisions at Jefferson Lab that made this evaluation of  $P_{11}(1440)$  and  $D_{13}(1520)$  electrocouplings possible. We are grateful to I. J. R. Aitchison, I. G. Aznauryan, R. G. Edwards, M. M. Giannini, T.-S. H. Lee, H.-W. Lin, C. D. Roberts, and E. Santopinto for helpful discussions. This work was supported in part by the U.S. Department of Energy and the National Science Foundation, the Russian Federation Government Grant 02.740.11.0242, 07.07.2009, the Skobeltsyn Institute of Nuclear Physics

and Physics Department at Moscow State University, University of South Carolina, Yerevan Physics Institute (Armenia), the Chilean Comisión Nacional de Investigación Científica y Tecnológica (CONICYT), the French Centre National de la Recherche Scientifique (CNRS), the French Commissariat à l’Energie Atomique, the Italian Istituto Nazionale di Fisica Nucleare, the National Research Foundation of Korea, and the UK Science and Technology Facilities Research Council (STFC), the Scottish Universities Physics Alliance (SUPA), and the United Kingdom’s Science and Technology Facilities Council. The Southeastern Universities Research Association (SURA) operates the Thomas Jefferson National Accelerator Facility for the United States Department of Energy under contract DE-AC05-84ER40150.

- 
- [1] I. G. Aznauryan and V. D. Burkert, *Prog. Part. Nucl. Phys.* **67**, 1 (2012).
  - [2] I. G. Aznauryan, V. D. Burkert, T.-S. H. Lee and V. I. Mokeev, *J. Phys: Conf. Ser.* **299**, 012008 (2011).
  - [3] V. D. Burkert, *Int. J. Mod. Phys. A* **26**, 493 (2011).
  - [4] V. D. Burkert, *Prog. Part. Nucl. Phys.* **55**, 108 (2005).
  - [5] V. D. Burkert and T. S. H. Lee, *Int. J. Mod. Phys. E* **13**, 108 (2004).
  - [6] G. V. Fedotov et al., CLAS Collaboration, *Phys. Rev. C* **79**, 015204 (2009).
  - [7] V. I. Mokeev et al., *Phys. Rev. C* **80**, 045212 (2009).
  - [8] S. J. Brodsky and S. D. Drell, *Phys. Rev. D* **22**, 2236 (1980).
  - [9] I. G. Aznauryan and A. S. Bagdasaryan, *Yad. Fiz.* **41**, 249 (1985).
  - [10] S. Capstick and B. D. Keister, *Phys. Rev. D* **51**, 3598 (1995).
  - [11] E. Pace, G. Salmé, and S. Simula, *Few Body Syst. Suppl.* **10**, 407 (1999); E. Pace, G. Salmé, F. Cardarelli, and S. Simula, *Nucl. Phys. A* **666**, 33 (2000).
  - [12] B. Juliá-Díaz, D. O. Riska, and F. Coester, *Phys. Rev. C* **69**, 035212 (2004).
  - [13] I. G. Aznauryan, *Phys. Rev. C* **76**, 025212 (2007).
  - [14] I. G. Aznauryan and V. D. Burkert, *Phys. Rev. C* **85**, 055202 (2012).
  - [15] I. G. Aznauryan et al., CLAS Collaboration, *Phys. Rev. C* **80**, 055203 (2009).
  - [16] S. Capstick and W. Roberts, *Progr. Part. Nucl. Phys.* **45**, S241 (2000).
  - [17] B. Julia-Diaz et al., *Phys. Rev. C* **77**, 045205 (2008).
  - [18] T.-S. H. Lee, *Int. J. Mod. Phys. E* **18**, 1215 (2009).
  - [19] B. Julia-Diaz et al., *Phys. Rev. C* **80**, 025207 (2009).
  - [20] H. Kamano et al., *Phys. Rev. C* **80**, 065203 (2009).
  - [21] H. Kamano et al., *Phys. Rev. C* **81**, 065207 (2010).
  - [22] N. Suzuki et al., *Phys. Rev. Lett.* **104**, 042302 (2010).
  - [23] N. Suzuki, T. Sato, and T.-S.H. Lee, *Phys. Rev. C* **82**, 045206 (2010).
  - [24] H. Kamano and T.-S. H. Lee, The 8th International Workshop on the Physics of Excited Nucleons, NSTAR2011, May 17-20, 2011, Newport News, VA, USA, ed. by V. Burkert, M. Jones, M. Pennington, D. Richards, AIP Conf. Proc, **1432**, 74.
  - [25] R. A. Arndt, J. M. Ford, and L. D. Roper, *Phys. Rev. D* **32**, 1085 (1985).
  - [26] R. A. Arndt, W. J. Briscoe, I. I. Strakovsky, and R. L. Workman, *Phys. Rev. C* **74**, 045205 (2006).
  - [27] S. Capstick et al., *Eur. Phys. J. A* **35**, 253 (2008).
  - [28] V. Braun et al., *Phys. Rev. Lett.* **103**, 072001 (2009).
  - [29] H.-W. Lin, *Chin. Phys. C* **33**, 1238 (2009).
  - [30] H.-W. Lin et al., *Phys. Rev. D* **78**, 114508 (2008).
  - [31] H.-W. Lin and S. D. Cohen, The 8th International Workshop on the Physics of Excited Nucleons, NSTAR2011, May 17-20, 2011, Newport News, VA, USA, ed. by V. Burkert, M. Jones, M. Pennington, D. Richards, AIP Conf. Proc, **1432**, 305.
  - [32] H.-W. Lin and S. D. Cohen, arXiv:1108.2528 [hep-lat].
  - [33] R. G. Edwards, J. J. Dudek, D. G. Richards, and S. J. Wallace, *Phys. Rev. D* **84**, 074508 (2011).
  - [34] J. J. Dudek and R. G. Edwards, *Phys. Phys. D* **85**, 054016 (2012).
  - [35] I. G. Aznauryan et al., arXiv:0907.1901 [nucl-th].
  - [36] G. Eichmann et al., *Phys. Rev. C* **79**, 065207 (2009).
  - [37] H.L.L. Roberts et al., *Few Body Syst.* **51**, 1 (2011).
  - [38] C. Chen, L. Chang, C. D. Roberts et al., arXiv:1204.2553[nucl-th].
  - [39] H. L. L., Roberts, Lei Chang, I. C. Cloet, and C. D. Roberts, Exclusive Reactions at High Momentum Transfer IV, Newport News VA, 18-21 May 2010, ed. by A. Radyushkin, World Scientific, 2011, p. 201.
  - [40] Lei Chang et al., *Phys. Rev. Lett.* **106**, 072001 (2011).
  - [41] D. J. Wilson, I. C. Cloet, L. Chang and C. Roberts, *Phys. Rev. C* **85**, 025205 (2012).
  - [42] K. Joo et al., CLAS Collaboration, *Phys. Rev. Lett.* **88**, 122001 (2002); K. Joo et al., CLAS Collaboration, *Phys. Rev. C* **68**, 032201 (2003); K. Joo et al., CLAS Collaboration, *Phys. Rev. C* **70**, 042201 (2004); H. Egiyan et al., CLAS Collaboration, *Phys. Rev. C* **73**, 025204 (2006); M. Ungaro et al., CLAS Collaboration, *Phys. Rev. Lett.* **97**, 112003 (2006); L. C. Smith et al., CLAS Collaboration, Proceedings of the Workshop “Shape of Hadrons”, p.222, Athens, 2006;

- K. Park et al., CLAS Collaboration, Phys. Rev. C **77**, 015208 (2008);  
A. Biselli et al., CLAS Collaboration, Phys. Rev. C **78**, 045204 (2008).
- [43] M. Ripani et al., CLAS Collaboration, Phys. Rev. Lett. **91**, 022002 (2003).
- [44] V. I. Mokeev et al., in “Proceedings of the 11th Workshop on the Physics of Excited Nucleons. NSTAR2007”, Springer 2008, ed. by H-W. Hammer, V. Kleber, U. Thoma, H. Schmieden, p. 76.
- [45] V. D. Burkert et al., Phys. Atom. Nucl. **70**, 427 (2007).
- [46] V. I. Mokeev et al., in “Proc. of the Workshop on the Physics of Excited Nucleon. NSTAR2005”, ed. by S. Capstick, V. Crede, P. Eugenio, World Scientific Publishing Co., p. 47.
- [47] I. G. Aznauryan et al., Phys. Rev. C **72**, 045201 (2005).
- [48] V. I. Mokeev and V. D. Burkert, J. Phys. Conf. Ser. **69**, 012019 (2007).
- [49] E. Byckling and K. Kajantie, “Particle Kinematics”, John Wiley & Sons 1972.
- [50] M. Ripani et al., Nucl. Phys. A **672**, 220 (2000).
- [51] I. J. R. Aitchison and J. J. Brehm, Phys. Rev. D **17**, 3072 (1978).
- [52] R. G. Newton, Scattering Theory of Waves and Particles, McGraw-Hill, 1969.
- [53] K. Nakamura et al., J. Phys. G, **37**, 075021 (2010).
- [54] D. Luke and P. Soding, Multiple Pion Photoproduction in the s Channel Resonance Region, Springer Tracts in Modern Physics 59 (1971).
- [55] I. J. R. Aitchison, Nucl. Phys. A **189**, 417 (1972).
- [56] D.M.Manley and E.M.Salesky, Phys. Rev. D **45**, 4002 (1992).
- [57] I. G. Aznauryan et al., Phys. Rev. C **71**, 015201 (2005).
- [58] V. D. Burkert et al., Phys. Rev. C **67**, 035204 (2003).
- [59] M. Dugger et al., CLAS Collaboration, Phys. Rev. C **79**, 065206 (2009).
- [60] L. Tiator, D. Drechsel, S. S. Kamalov, and M. Vanderhaeghen, Eur. Phys. J. ST **198**, 141 (2011).
- [61] L. Tiator, D. Drechsel, S. S. Kamalov, and M. Vanderhaeghen, Chinese Phys. C **33**, 1069 (2009).
- [62] L. Tiator, D. Drechsel, S. S. Kamalov, Eur. Phys. J. A **34**, 69 (2007).
- [63] Zp. Li, V. Burkert, and Zh. Li, Phys. Rev. D **46**, 70 (1992).
- [64] S. D. Drell and T. M. Yan, Phys. Rev. Lett. **24**, 181 (1970).
- [65] V. B. Berestetskii and M. V. Terent’ev, Sov. J. Nucl. Phys. **24**, 1044 (1976); **25**, 347 (1977).
- [66] B. D. Keister and N. W. Polyzou, Adv. Nucl. Phys. **20**, 225 (1991).
- [67] G. Ramalho and K. Tsushima, Phys. Rev. D **81**, 074020 (2010).
- [68] F. Gross, J. W. Van Orden, and K. Holinde, Phys. Rev. C **45**, 2094 (1992).
- [69] F. Gross, G. Ramalho, and M. T. Pena, Phys. Rev. C **77**, 015202 (2008).
- [70] T. Sato and T.-S. H. Lee, Phys. Rev. C **54**, 2660 (1996).
- [71] T. Sato and T.-S. H. Lee, Phys. Rev. C **63**, 055201 (2001).
- [72] B. Julia-Diaz et al., Phys. Rev. C **75**, 015205 (2007).
- [73] T. Sato and T.-S. H. Lee, J. Phys. G **36**, 055201 (2009).
- [74] Fl. Stancu and P. Stassart, Phys. Rev. D **39**, 343 (1989).
- [75] P. Stassart and Fl. Stancu, Z. für Phys. A **351**, 77 (1995).
- [76] I. T. Obukhovskiy et al., Phys. Rev. D **84**, 014004 (2011).
- [77] M. Aiello, M. M. Giannini and E. Santopinto, J. Phys. G **24**, 753 (1998).
- [78] G. F. de Teramond and S. J. Brodsky, The 8th International Workshop on the Physics of Excited Nucleons, NSTAR2011, May 17-20, 2011, Newport News, VA, USA, ed. by V. Burkert, M. Jones, M. Pennington, D. Richards, AIP Conf. Proc. **1432**, 168.
- [79] R. Koniuk and N. Isgur, Phys. Rev. D **21**, 1868 (1980).
- [80] S. Capstick and W. Roberts, Phys. Rev. D **49**, 4570 (1994).
- [81] M. Jacob and G. C. Wick, Ann. of Phys. **7**, 404 (1959).



### Appendix A: Resonance hadronic decay amplitudes employed in the JM model

The relationship within the JM model [7, 50] between the  $N^*$  hadronic decay amplitudes  $\langle \lambda_f | T_{dec} | \lambda_R \rangle$  and the energy-dependent  $N^*$  partial hadronic decay widths  $\Gamma_{\lambda_f}(W)$  is presented in this Appendix. Here  $\lambda_R$  is the helicity of the ' $N^*$ ', which decays into  $\pi\Delta$  or  $\rho p$  final states with helicity  $\lambda_f$ .

The  $N^*$  hadronic decay amplitudes in Eq. (2) can be expanded in partial waves of total momentum  $J$ :

$$\langle \lambda_f | T_{dec} | \lambda_R \rangle = \sum_J \langle \lambda_f | T_{dec}^J | \lambda_R \rangle d_{\mu\nu}^J(\cos \theta^*) e^{i\mu\phi^*}, \quad (17)$$

where  $\theta^*$  and  $\phi^*$  are the CM emission angle of the  $\pi$  for the  $\pi\Delta$  intermediate state and of the final ' $p$ ' for the  $\rho p$  intermediate states. The indexes  $\mu$  and  $\nu$  are defined in Eq. (3). Only a single term with  $J=J_r$ , where  $J_r$  is resonance spin, contributes to the expansion in Eq. (17) because of total angular momentum conservation. We can rotate the quantization axis adopted for the initial-state  $|\lambda_R\rangle$  wave function and re-evaluate the matrix element  $\langle \lambda_f | T_{dec} | \lambda_R \rangle$  in the frame with the quantization axis defined by the final  $\pi$  (the final ' $p$ ') momentum for  $\pi\Delta$  ( $\rho p$ )  $N^*$  decays, respectively. The matrix element  $\langle \lambda_f | T_{dec} | \lambda_R \rangle$  after rotation becomes:

$$\langle \lambda_f | T_{dec} | \lambda_R \rangle = \sum_{\nu'} \langle \lambda_f | T_{dec} | J_r \nu' \rangle d_{\mu\nu'}^{J_r}(\cos \theta^*) e^{i\mu\phi^*}. \quad (18)$$

The superposition of the states  $|J_r \nu'\rangle$  in Eq. (18), with spin  $J_r$  and projection onto the final-state quantization axis  $\nu'$ , is the transformed wave function of the initial-state  $|\lambda_R\rangle$  after the aforementioned rotation of the initial-state quantization axis. Rotational invariance of the resonance hadronic decay amplitudes requires that the operator  $T_{dec}$  should be an  $SU(2) \otimes O(3)$  - spin  $\otimes$  orbital momentum scalar. Only the term with  $\nu' = \nu$  in Eq. (18) (with  $\nu$  defined by Eq. (3)) remains non-zero in the sum of Eq. (18), as a consequence of the Wigner-Eckart theorem applied to matrix elements  $\langle \lambda_f | T_{dec} | J_r \nu' \rangle$  with the scalar  $T_{dec}$  operator.

From comparisons between Eqs. (17) and (18) we can see that:

$$\langle \lambda_f | T_{dec}^{J_r} | \lambda_R \rangle = \langle \lambda_f | T_{dec} | J_r \nu \rangle, \quad (19)$$

The  $\langle \lambda_f | T_{dec}^{J_r} | \lambda_R \rangle$  matrix elements in Eqs. (3,19) are determined by the final-state helicity  $\lambda_f$  only, and are independent of  $N^*$  helicities  $\lambda_R$ .

Assuming real values for the matrix element  $\langle \lambda_f | T_{dec}^{J_r} | \lambda_R \rangle$  in Eqs. (3,19), we can relate it to the  $\Gamma_{\lambda_f}(W)$  partial hadronic decay width of the excited state  $N^*$  to the final state of helicity  $\lambda_f$ . We employ general relations of quantum theory between the resonance decay amplitude  $\langle \lambda_f | T_{dec} | \lambda_R \rangle$  of Eq. (17), the two-body state phase space of resonance decay products  $d\Phi_{2b}$ , and the  $\Gamma_{\lambda_f}(W)$

decay width:

$$\Gamma_{\lambda_f}(W) = \frac{1}{2M_r} \frac{1}{2J_r + 1} \sum_{\lambda_R} \int |\langle \lambda_f | T_{dec} | \lambda_R \rangle|^2 d\Phi_{2b}. \quad (20)$$

The factor  $\frac{1}{2M_r}$  in Eq. (20) reflects the spin-tensor normalization in the convention of the JM model [7]. This normalization, and the expression for the ' $S$ '-matrix adopted in the JM model [7], defines the final-state two-body phase space  $d\Phi_{2b}$  as:

$$\begin{aligned} d\Phi_{2b} &= \frac{1}{4\pi^2} \frac{p_f}{4M_r} \sin(\theta^*) d\theta^* d\phi^*, \\ E_f &= \frac{W^2 + M_f^2 - M_{f'}^2}{2W}, \\ p_f &= \sqrt{E_f^2 - M_f^2}, \end{aligned} \quad (21)$$

where  $E_f$ ,  $p_f$  are the energy and momentum modulus of one of the final hadrons  $f$  ( $f$  is either pion or the final proton for the  $N^* \rightarrow \pi\Delta$  or  $\rho p$  decays, respectively),  $M_f$  is its mass, while the index  $f'$  stands for the other hadron. All frame-dependent kinematic variables of the final hadrons are defined in the final hadron CM frame. Inserting Eqs. (17,19) into Eq. (20) and accounting for and the ' $d$ '-function normalization,

$$\int d_{\mu\nu}^{J_r}(\cos \theta^*) \cdot d_{\mu\nu}^J(\cos \theta^*) \sin \theta^* d\theta^* = \frac{2}{2J+1}, \quad (22)$$

we obtain Eq. (3) for the  $\langle \lambda_f | T_{dec} | \lambda_R \rangle$  amplitudes, apart from the factor  $\sqrt{\frac{\langle p_i^r \rangle}{\langle p_i \rangle}}$ . Note that at the resonant point,  $W=M_r$ , this factor is equal to unity. However, in calculations of resonant cross sections for  $W \neq M_r$ , the two-body phase space becomes different than that at the resonant point. The factor  $\sqrt{\frac{\langle p_i^r \rangle}{\langle p_i \rangle}}$  in Eq. (3) accounts for this difference. It is needed to evaluate resonant cross sections and amplitudes for  $W$  values off the resonant point.

The  $\langle p_i^r \rangle$  and  $\langle p_i \rangle$  absolute three-momentum values of the final  $\pi$  for the  $N^* \rightarrow \pi\Delta$  decay ( $i=1$ ) or of the final  $p'$  for the  $N^* \rightarrow \rho p$  decay ( $i=2$ ) in Eq. (3) are averaged over the running mass of the unstable hadron in the intermediate state:

$$\langle p_i^r \rangle = \int dM_i^2 \frac{1}{\pi} \frac{M_{i0} \Gamma_{i0}}{(M_i^2 - M_{i0}^2)^2 + M_{i0}^2 \Gamma_{i0}^2} p_i^r(M_i^2), \quad (23)$$

$$\langle p_i \rangle = \int dM_i^2 \frac{1}{\pi} \frac{M_{i0} \Gamma_{i0}}{(M_i^2 - M_{i0}^2)^2 + M_{i0}^2 \Gamma_{i0}^2} p_i(M_i^2),$$

where  $M_i$  is the current invariant mass of the final  $\pi p$  particles in the case of  $N^* \rightarrow \pi\Delta$  decay ( $i=1$ ) or the current invariant mass of final  $\pi\pi$  particles for the  $N^* \rightarrow \rho p$  decay ( $i=2$ );  $M_{i0}$  are the central masses of either  $\Delta$  ( $i=1$ ) or  $\rho$  ( $i=2$ ); and  $\Gamma_{i0}$ , are their total decay

widths. The running momenta of the stable particles from  $N^*$  decays  $p_i(M_i^2)$  in Eq. (23) are evaluated as:

$$p_1 = \frac{[(W^2 + m_\pi^2 - M_1^2)^2 - 4W^2 m_\pi^2]^{1/2}}{2W} \text{ and} \quad (24)$$

$$p_2 = \frac{[(W^2 + m_{p'}^2 - M_2^2)^2 - 4W^2 m_{p'}^2]^{1/2}}{2W}.$$

The values of these momenta at the resonance point  $p_i^r(M_i^2)$  were obtained from Eq. (24) at  $W = M_r$ .

The hadronic decay widths  $\Gamma_{\lambda_f}(W)$  were taken from experiments with hadronic probes, as was described in Section III. Those decay widths were obtained in another representation of orbital angular momentum  $L$  and total final hadron spin  $S$   $\Gamma_{LS_f}(W)$ . The partial  $\Gamma_{\lambda_f}(W)$  decay widths can be transformed into this representation [81] by:

$$\sqrt{\Gamma_{\lambda_f}} = \sqrt{\frac{2J_r + 1}{2L + 1}} \langle L0S\lambda_1 - \lambda_2 | J_r \lambda_1 - \lambda_2 \rangle \cdot$$

$$\langle s_1 \lambda_1 s_2 - \lambda_2 | S \lambda_1 - \lambda_2 \rangle \sqrt{\Gamma_{LS}}, \quad (25)$$

where  $s_1, \lambda_1, s_2, \lambda_2$  are spins and helicities for first stable and second unstable particles in the intermediate states.